Swiss Journal of Geosciences (2019) 112:597–617
https://doi.org/10.1007/s00015-019-00351-4

Electron microprobe petrochronology of monazite-bearing garnet micaschists in the Oetztal-Stubai Complex (Alpeiner Valley, Stubai)

Bernhard Schulz[1] · **Joachim Krause**[2] · **Robert Zimmermann**[3]

Received: 22 March 2018 / Accepted: 22 October 2019 / Published online: 8 November 2019

Abstract

Monazite dating in metapelites is an emerging method to investigate polymetamorphic areas. A protocol for Th–U–Pb dating of monazite by electron microprobe was adopted for a JEOL JXA-8530F. It was applied to the Variscan and Early-Alpine metamorphic Austroalpine Oetztal-Stubai Complex (OSC). In the Alpeiner Valley in the Stubai region, the Schrankogel complex is the eastern succession of the Central Metabasite Zone. In this part, metabasites are alternating with metapelites. In 4 samples from micaschist lenses, dominantly Carboniferous monazite isochrone ages at 335 ± 4 Ma, 320 ± 4 Ma; 319 ± 4 Ma and 319 ± 4 Ma were obtained. The micaschist samples with diverse modal compositions and variable bulk rock Ca contents of calculated assay, display distinct monazite microstructures, as quantified by automated SEM-MLA (mineral liberation analysis) routines. Clusters of small monazite could indicate new crystallization and yielded isochrones at 313 and 304 Ma. In contrast, corona structures of apatite and allanite around large monazites with isochrones between 350 and 315 Ma suggest a decomposition during decreasing temperature. Garnets in metapelitic assemblages display growth zonations with low pyrope contents in the cores and pyrope-rich rims. A prograde metamorphism with high pressure amphibolite-facies peak conditions at ~ 12 kbar and ~ 680 °C, and a post P_{max} path with decompression to 4 kbar and 640–600 °C was estimated from the micaschists and from zoned Ca-amphiboles in retrogressed amphibolitized eclogites. The P–T path entered the monazite stability field during the decompression. This signals a Carboniferous age of the metamorphism. A minor population in one sample is composed of sporadic Permian single monazite ages. A Cretaceous monazite population is lacking. In the wide parts of the Austroalpine basement with Carboniferous-to-Cretaceous mica mixing ages, monazite age populations allow to discriminate a distinct Permian metamorphic event.

Keywords Th–U–Pb-monazite dating · Geothermobarometry · Automated SEM mineral liberation analysis · Variscan · Austroalpine basement · Eastern Alps

Editorial Handling: E. Gnos.

Electronic supplementary material The online version of this article (https://doi.org/10.1007/s00015-019-00351-4) contains supplementary material, which is available to authorized users.

✉ Bernhard Schulz
Bernhard.Schulz@mineral.tu-freiberg.de

Joachim Krause
joachim.krause@hzdr.de

Robert Zimmermann
r.zimmermann@hzdr.de

[1] Division of Economic Geology and Petrology, Institute of Mineralogy, TU Bergakademie Freiberg, Brennhausgasse 14, 09599 Freiberg, Saxony, Germany

[2] Department of Analytics, Helmholtz-Zentrum Dresden-Rossendorf, Helmholtz Institute Freiberg for Resource Technology, Chemnitzer Straße 40, 09599 Freiberg, Saxony, Germany

[3] Department of Exploration, Helmholtz-Zentrum Dresden-Rossendorf, Helmholtz Institute Freiberg for Resource Technology, Chemnitzer Straße 40, 09599 Freiberg, Saxony, Germany

1 Introduction

A major part of the Eastern Alps is composed of basement units with a polymetamorphic history. Early Palaeozoic, Carboniferous and Permian events, and the Alpine Cretaceous and Cenozoic metamorphism have been reported from the various Austroalpine and Penninic realms (Frey et al. 1999). The Austroalpine Oetztal-Stubai Complex (OSC) in the Central Alps is one of the classical areas of polymetamorphism (Purtscheller 1978; Thöni 1999; Frisch et al. 2000). Various isotopic dating methods have been applied there. An Early Palaeozoic high-temperature anatectic event was reported from the Winnebach, Verpeil and Klopaier migmatites (Klötzli-Chowanetz et al. 1997, 2001; Neubauer et al. 1999; Söllner 2001; Thöny et al. 2008). Eclogite-facies and amphibolite-facies conditions were attained during the Variscan (Devonian-Carboniferous) metamorphism (Mogessie et al. 1985; Miller and Thöni 1995; Mogessie and Purtscheller 1986; Tropper and Hoinkes 1996; Rode et al. 2012). The Variscan metamorphic overprint led to kyanite, sillimanite and andalusite mineral zones (Fig. 1b) of which boundaries cut across and postdate the large-scale Schlingen structures of the regional foliation (Purtscheller 1978). The chloritoid and staurolite isograds, and the NW boundary of Alpine biotite ages are also discordant to the Schlingen structures and general trends of the foliation (Fig. 1b).

In many parts of the Austroalpine basement, Permian ages of mica were formerly interpreted as Carboniferous-to-Cretaceous "mixing ages" (Thöni 1981). These days, such Permian magmatic and metamorphic ages are considered to indicate a distinct geodynamic event, namely a post-collisional HT-LP metamorphism (Schuster et al. 2001; Marotta and Spalla 2007; Schuster and Stüwe 2008). In the OSC, an increasing grade of an Early Alpine (Cretaceous) overprint towards the South has been described (Thöni 1981, 1983; Hoinkes et al. 1991, 1999; Hoinkes and Thöni 1993; Thöni 1999). This is obvious from Variscan-to-Alpine K–Ar and Rb–Sr "mixed ages" of mica, changing to Cretaceous ages towards the SE. The successive occurrence of chloritoid and then staurolite towards the Schneeberg and Texel Complexes (Fig. 1b), accompanied by distinct growth zones in garnet porphyroblasts (Frank et al. 1987; Tropper and Recheis 2003) are also assigned to this Early Alpine overprint. The Late Alpine (Cenozoic) events with South Alpine indenter and lateral extrusion led to faults and shear zones which reframe and dissect the OSC. The main tectonic lines are the sinistral Inntal fault zone to the North, the Brenner normal fault zone to the East, the Schneeberg fault zone and Vinschgau shear zone to the South, the Schlinig zone to the West, and the Engadine line to the Northwest (Ratschbacher et al. 1991; Frisch et al. 2000; Schmid et al. 2004).

In this context, the OSC represents a difficult situation for the resolution of the thermal events by age dating. Dependent on metamorphic grade and P–T paths, Rb–Sr, K–Ar and Ar–Ar methods can provide ages on the cooling history of the latest amphibolite- to greenschist-facies metamorphic event. The Carboniferous-to-Cretaceous mica "mixing ages" may hide or mask a distinct Permian thermal event. Methods based on U–Pb in zircon mostly fail, as the corresponding closure temperature and formation temperatures have not been achieved during amphibolite-facies and eclogite-facies metamorphism. Other methods as Sm–Nd and Lu–Hf in metamorphic garnet are difficult in specific applications and rarely available (Hauke et al. 2019). In this frame, the electron microprobe (EMP) Th–U–Pb monazite dating in metapelites appears to be promising (Williams et al. 2017). Here, we report a protocol for Th–U–Pb monazite dating and mineral chemical analysis with a JEOL JXA-8530F electron microprobe, applied to metapelites from the Alpeiner Valley in the Stubai area of the OSC. The monazite ages and the P–T evolution in this part of the OSC turned out to be similar to corresponding data from adjacent areas which indicate a Variscan (Carboniferous) clockwise P–T evolution. The monazites in the Alpeiner Valley apparently crystallised and were dissipated in diverse microstructures during the decompression path.

2 Geological setting and petrography

In the Alpeiner Valley around the Franz-Senn-Hütte in the NE part of the OSC, a succession from metapsammites and metapelites in the southern part, to an amphibolite dominated northern part of a "Wechselserie" is observed. Metagranitoids occur within this sequence (Fig. 2). Previous regional petrographic and tectonic studies (Hammer 1929; Purtscheller 1978; Schulz 1994; Rode et al. 2012; Egglseder and Fügenschuh 2013) cover the NE part of the OSC, but details are lacking for the Alpeiner Valley. The Alpeiner Valley and its metamorphic lithology have been recently described and labelled by Klötzli-Chowanetz (2016) and Palzer (2016). Accordingly, the Schrankogel complex (the former Alpeiner Metabasitzone in Schindlmayr (1999)), is composed mainly of amphibolites and biotite hornblende gneisses and forms the eastern succession of the Central Metabasite Zone (CMB) of the OSC. Protoliths of the CMB are gabbros and basalts with MORB-chemistry (Mogessie et al. 1985) and Early Cambrian ages (Miller and Thöni 1995), emplaced in a back-arc setting. The CMB is subdivided from N to S into five zones (Hoernes and Hoffer 1973; Purtscheller 1978): (1) Roughly foliated amphibolite with layers and lenses of eclogite and rare peridotite, (2) Dark, garnet-bearing amphibolites, (3)

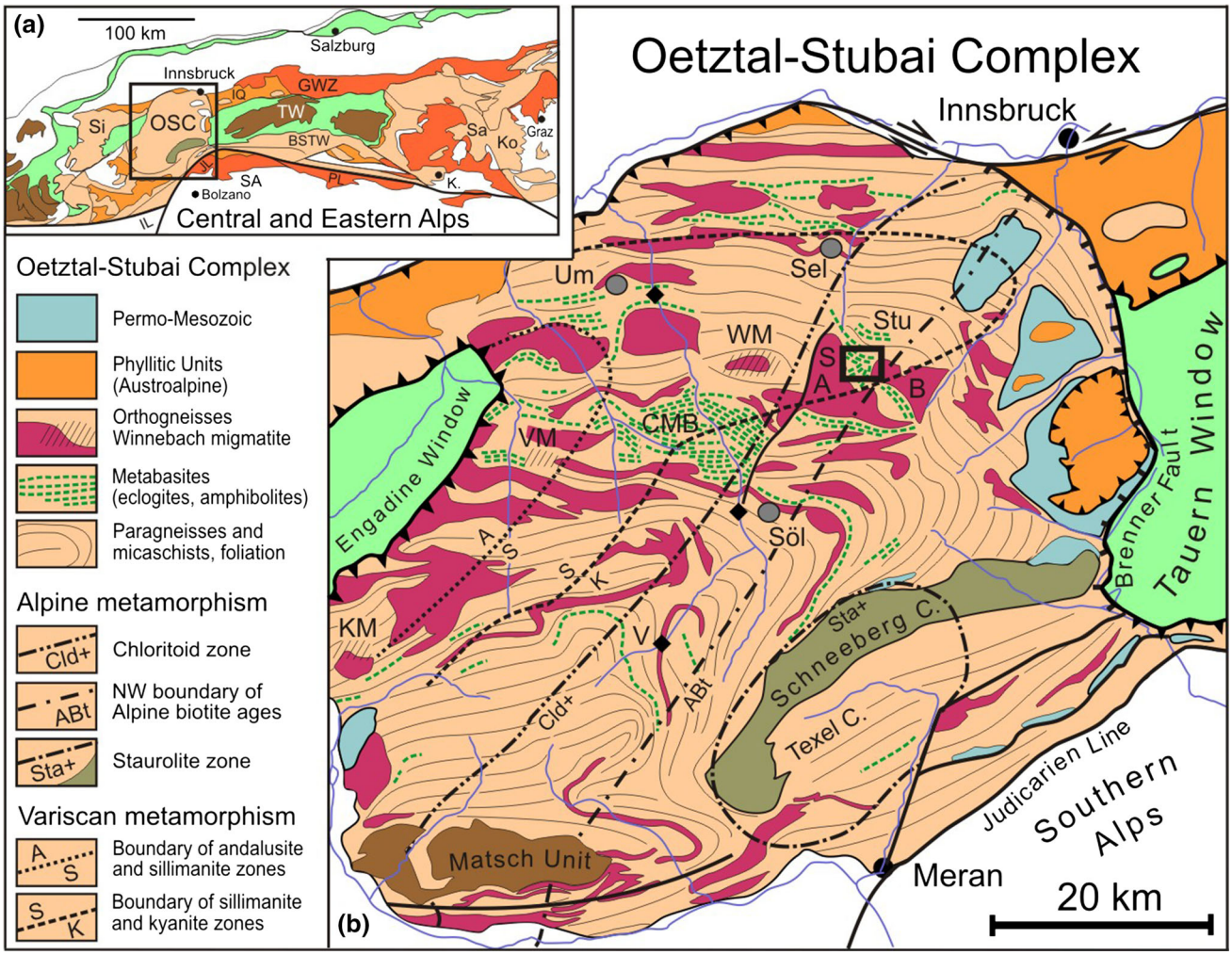

Fig. 1 **a** Location of the study area in the basement units of the Central and Eastern Alps: *BSTW* Basement South of Tauern Window, *GWZ* Graywacke Zone, *IL* Insubric Line, *IQ* Innsbrucker Quartzphyllite, *JL* Judicarien Line, *Ko* Koralpe, *OSC* Oetztal-Stubai Complex, *PL* Periadriatic Lineament, *Sa* Saualpe, *SA* South Alpine, *Si* Silvretta, *TW* Tauern Window (Penninic Unit). **b** Geological sketch map of the Oetztal-Stubai basement in the Central Alps, redrawn after Schmidegg (1964), with the various additions by Miller et al. (1967) and Purtscheller (1978), with Variscan mineral zones and domains of Alpine Cretaceous metamorphism after Thöni (1981), Frank et al. (1987) and Hoinkes and Thöni (1993). Study area around the Franz-Senn-Hütte in the Stubai Alps (Stu) is marked by square. *A* Alpeiner metagranodiorite, *B* Bassler metagranite, *CMB* Central Metabasite Zone, *KM* Klopeiner migmatite, *VM* Verpeil migmatite, *WM* Winnebach migmatite, *S* Schrankogel complex with metabasites. Sampling areas in Rode et al. (2012) are Sellrain (Sel), E of Sölden (Söl), and W of Umhausen (Um) around Erlanger Hütte. Vent (V) is situated in the area with large-scale Schlingen structures

Alumosilicate gneisses, (4) "Wechselserie", and (5) Southern eclogite zone. The Schrankogel complex with its metabasites alternating with metapelites to metapsammites could be correlated to the "Wechselserie" as outlined by Hoernes and Hoffer (1973) and Purtscheller (1978).

The host rocks of the metabasites are former clastic sequences with presumably Neoproterozoic deposition ages. In the study area these meta-psammopelitic rocks are composed of quartzites and staurolite bearing micaschists and paragneisses. In the northern part, micaschists form lenses within the"Wechselserie" of the Schrankogel complex, often not extending more than 50 × 20 m. Four micaschist samples were selected for monazite analyses and two of them served for geothermobarometry (Fig. 2). The general mineral assemblage is quartz, plagioclase, muscovite, biotite, and garnet. Staurolite, sometimes twinned and up to 2 mm in size, can be observed in samples RZ31, RZ33 and RZ42. Accessories are tourmaline, sphene, ilmenite, zircon and monazite. Sample RZ29 shows strong retrogression of biotite completely replaced by chlorite. Garnet is partially to completely replaced by chlorite, while staurolite is replaced by large sericite pseudomorphs. In sample RZ31 with well-preserved biotite and numerous small garnet, relics of staurolite remained in the sericite pseudomorphs. In sample RZ33 the large garnet porphyroblasts (up to 5 mm in diameter) are accompanied

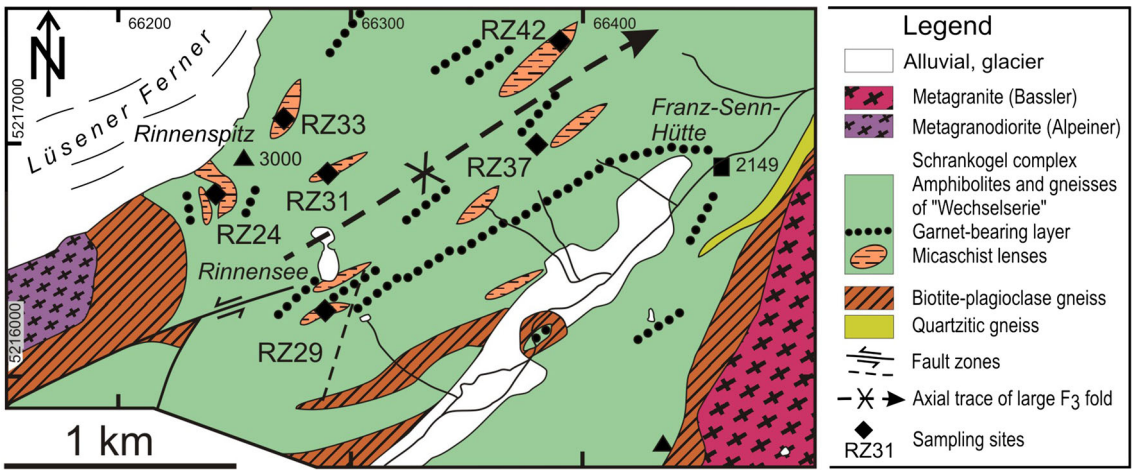

Fig. 2 Geological sketch map of the Schrankogel complex in the area W of Franz-Senn-Hütte in the Alpeiner Valley, Austroalpine Oetztal-Stubai basement, with sampling locations referred to in the text. Alpeiner metagranodiorite and Bassler metagranite

by staurolite and kyanite which are partly sericitised in the foliated matrix. In sample RZ42 the large garnet porphyroblasts (up to 6 mm in diameter) enclose staurolite in their rims. Kyanite and staurolite occur in the foliated matrix (Table 1).

The variety of the Schrankogel complex metabasites ranges from amphibolitized eclogite, garnet-amphibolite and amphibolite to biotite-hornblende-gneiss with folded layers of calcsilicate gneiss. The unit shows in mean a smooth, zonal, anastomosing, sometimes gradational foliation. Amphibolitized eclogite can be observed in small, often altered lenses elongated several meters in the northern part. Clinopyroxene and plagioclase appear exclusively in coarse-grained symplectites. Primary Na-rich clinopyroxene has not been found in the Schrankogel complex and is apparently restricted to the eclogite occurrences in the western part of the Central Metabasite Zone (Miller and Thöni 1995; Rode et al. 2012). Garnet displays sieve-like internal structures and is often replaced by mica and feldspar. The amphibolites and hornblende gneisses are mainly composed of green amphibole and plagioclase. Plagioclase often displays saussuritisation. Green amphibole has actinolite and chlorite fringes. Garnet up to 2 cm in diameter overgrows the foliated main fabric, indicating a crystallization at a late stage.

3 Structures and tectonic setting

The Oetztal-Stubai basement can be divided into two main tectonic domains (Purtscheller 1978; Egglseder and Fügenschuh 2013): (1) Pre-Mesozoic large amplitude open folds in the northern part and (2) the large-scale Schlingen-structures in the southwestern part around Vent. In the studied area with its intermediate position between these structural parts of the OSC (Fig. 1), a large synclinal fold structure with a gently NE plunging axis and vergence to the S is the main structure (Fig. 2). It deforms a steeply N- and S-dipping main foliation. Our field description and labelling of the regional tectonic structures is affiliated to concepts which have been applied to similar Austroalpine basement areas with a pre-Alpine evolution, as the basement south of the Tauern Window (Schulz et al. 2008). Accordingly, monomineralic quartz layers in metapelites are considered to represent an older foliation S_1. These quartz layers S_1 display cm-scale intrafolial isoclinal folding F_2. Also one can observe m-scale isoclinal folds F_2. The main foliation S_2 is axial-planar to these F_2 folds. Subsequently, the main foliation S_2 was deformed in F_3 folds at all scales. Parasitic folds F_3 are minor structures of a large-scale South-vergent F_3 fold. The geometrical interpretation of the S_2 main foliation planes in the Alpeiner Valley reveals a 5 km scale cylindric fold with a fold axis slightly plunging to NE (Fig. 2). The π-pole at 024/27 was calculated by a Bingham axial distribution (cylindrical best fit) with OSX Stereonet (Cardozo and Allmendinger 2013). The calculated π-pole coincides with the 95% confidence interval of the measured second order fold axes F_3. The smaller scale second order folds F_3 are outstandingly visible in the units of the "Wechselserie", where they are composed of calcsilicates or monomineralic quartz layers. The overprinting of the isoclinal F_2 folds by F_3 folding led to a mixed type 2/3 fold interference pattern (Ramsay and Huber 1987; Egglseder and Fügenschuh 2013). In their detailed tectonic study of the area, Egglseder and Fügenschuh (2013) described the similar structures and geometries, but introduced a different subscript labelling. The large-scale F_3 folds deforming S_2 as labelled here, correspond to the D_2 folds in Egglseder and Fügenschuh (2013). As the S_2 and F_3 fold structures, and D_2

Table 1 Results from automated SEM Mineral Liberation Analysis (MLA) of petrographic thin sections of monazite-bearing garnet micaschist samples from the Alpeiner Valley, Stubai region. Modal mineralogy of major phases, from XMOD point counting routine with ~ 10^6 EDX analyses per thin section. Ca and Al bulk rock compositions in wt%, as calculated assay from modal mineralogy. Area, number of grains and grain size as MD50 (grain size at 50 wt% of cumulative grain size distribution) in µm for zircon (Zrn), monazite (Mnz) and xenotime (Xtm) from automated SEM Spare Phase Lineup (SPL) routine. The monazite grains are in contact with diverse other phases, as biotite (Bt), plagioclase (Pl), quartz (Qtz), apatite (Ap) and ilmenite (Ilm). These microstructural relationships are reported as ternary locking in %. Note high degree of ternary locking of monazite with allanite (Aln) and epidote (Epi) in sample RZ29 with corona structures

Mineral	RZ29	RZ31	RZ33	RZ42
Quartz wt% XMOD	22.51	25.66	25.39	26.63
Albite + K-feldspar	7.47	3.90	9.72	2.21
Plagioclase	2.05	18.27	23.24	5.53
Biotite	1.60	15.55	7.65	4.47
Chlorite	15.10	4.65	6.46	2.89
Muscovite	31.40	23.70	6.11	27.88
Garnet	14.21	4.11	12.71	19.42
Staurolite	0.00	1.96	1.30	6.59
Epidote	2.33	0.49	3.82	0.32
Apatite	0.52	0.27	0.66	0.18
Area (10^6µm^2)	293	173	269	318
Ca bulk wt% calc	1.10	0.89	2.04	0.92
Al bulk wt% calc	10.81	9.94	8.34	11.41
Zircon SPL (µm^2)	192,229	116,786	209,182	436,128
Xenotime SPL (µm^2)	221	4053	4754	1146
Monazite SPL (µm^2)	8306	72,675	34,580	110,212
Zrn grains (SPL)	904	638	1103	1347
Zrn size MD50 (µm)	25	23	22	50
Xtm grains (SPL)	2	38	32	6
Xtm size MD50 (µm)	12	14	22	24
Mnz grains (SPL)	23	292	142	36
Mnz size MD50 (µm)	42	30	22	95
Mnz ternary locking				
Locked in Bt (%)	49.25	37.59	25.14	61.41
Locked in Pl	0.52	27.79	23.65	0.22
Locked in Qtz	6.4	19.04	2.8	2.82
Locked in Aln + Epi	32.63	5.45	18.37	3.91
Locked in Ap	3.07	0.83	2.16	0
Locked in Ilm	0.12	0.38	14.71	3.46
Mnz microstructure	Corona	Cluster	Corona	Large
Age ± wght.av. (Ma)	335 ± 4	319 ± 4	320 ± 4	319 ± 3

respectively, are not observed in the Brenner Mesozoic (Purtscheller 1978; Egglseder and Fügenschuh 2013), they should belong to pre-Mesozoic and pre-Alpine events. Also mineral cooling ages (Thöni 1999) imply no Alpine (Cretaceous) metamorphic event with ductile deformation in the northern parts of the Oetztal-Stubai Complex. The subsequent Alpine deformation phases display an increasing brittle component (Egglseder and Fügenschuh 2013): W to NW directed thrusts are related to a Cretaceous thrusting. This stage is not observed in the study area. A subsequent top-to-SE directed shearing, appears to be related to a late Cretaceous extension. This stage is observed in the two-mica porphyroblastic gneiss in the south-eastern part of the study area. Several phases of brittle deformations in the studied area were related to Miocene to Neogene lateral extrusion and exhumation of the Tauern Window (Ratschbacher et al. 1991; Egger 1997).

4 Analytical methods

4.1 SEM-based automated mineralogy (MLA)

Automated mineralogical methods (e.g. Fandrich et al. 2007), based on a scanning electron microscope SEM Quanta 650-FEG-MLA by FEI Company, equipped with Bruker Dual X-Flash energy dispersive spectrometers for EDX analyses were applied to complete thin sections of garnet micaschists, as described in Schulz (2017). Acceleration voltage of the focussed electron beam was set at 25 kV. Beam current was adjusted at 10 nA. A software package for mineral liberation analysis (MLA version 2.9.0.7 by FEI Company) was used for the automated steerage of the electron beam for EDX identification of mineral grains and collection of numerous EDX spectra. Then follow the measurement routines given below:

1. XMOD is a single spot point counting for mineral mode analysis, based on ~ 10^6 EDX spectra at a 10 µm step size in a thin section. Mineral modes in wt% (Table 1) have been recalculated by introducing average densities listed in mineral databases. A calculated chemical assay was derived from the mineral mode, densities, and the mineral chemical compositions. For garnet, biotite, muscovite, and plagioclase the representative compositions from EDX and EPMA measurements were introduced. The calculated assays (Table 1) thus represent an approximation to the bulk rock composition in a given thin section plane and may differ from the bulk composition obtained from a larger volume of rock.
2. The SPL (Selected Phase Lineup) routine combines a backscattered electron (BSE) grey colour value trigger and single spot EDX-ray spectral analysis. This enables the detection of rare phases as monazite, xenotime and zircon and their surrounding minerals. One receives a catalogue of all monazite and xenotime intermineral

relationships (Table 1). This was used to select monazite grains for detailed investigation in backscattered electron imageing under the SEM, and quantitative WDS analysis with the electron microprobe (EPMA).

3. The GXMAP routine produces a narrow grid of ~ 1600 single EDX-ray spectra per mm^2, at a stepsize of 25 µm. Garnet and biotite in samples RZ33 and RZ42 were chosen as the target phases. For the classification of mineral phases and compositions in XMOD, SPL and GXMAP measurements, a list of identified reference EDX-ray spectra was established by collecting spectra from matrix phases and from defined parts of several garnet porphyroblasts (core—mid—rim). It is indispensable to use sample garnets for this procedure, as the spectra from the available standard garnets and arbitrary other garnet-bearing rocks will not match due to different element compositions. Garnet reference spectra are further characterized by EDX-ray single spot elemental analyses which revealed strong variations of Fe, Mg, Mn and Ca in the porphyroblasts. In a next step, the reference spectra were labelled in a generic way with the corresponding garnet Fe–Mg-Mn–Ca compositions. When the labelled spectra are arranged in a color scale, they correspond to semi-quantitative garnet zoning maps. The GXMAP measurements were classified against the reference EDX-ray spectra list with a high degree of probability of match (Schulz 2017). The GXMAP measurements allowed to select garnets with a well-developed and complete concentrical element zonation out of dozens of porphyroblasts for quantitative WDS analysis with electron microprobe (EPMA).

4.2 Electron microprobe (EPMA) and monazite dating

The mineral-chemical analyses from metabasite and metapelite samples were performed with a JEOL JXA-8900-RL instrument at beam conditions of 15 kV, 20 nA, 2 µm, and with the corresponding ZAF correction procedures. The ~ 900 analytical points on garnet, mica, feldspar, amphibole, clinopyroxene and epidote from the metapelite and metabasite samples enclose detailed garnet zonation traverses.

Electron microprobe Th–U–Pb dating is based on the observation that common Pb in monazite (LREE, Th)PO_4 is negligible when compared to radiogenic Pb resulting from the decay of Th and U (Parrish 1990; Montel et al. 1996). Electron microprobe analysis of the bulk Th, U and Pb concentrations in monazite, at a constant $^{238}U/^{235}U$, allows for the calculation of an isochron age (Suzuki and Adachi 1991; Suzuki and Kato 2008) and/or for single domain ages with a considerable error (Montel et al. 1996; Pyle et al. 2005; Jercinovic et al. 2008; Spear et al. 2009; Williams et al. 2017). A protocol for the monazite analysis with a JEOL JXA-8530F electron microprobe hosted at the Helmholtz Institute Freiberg for Resource Technology has been developed. Some parts of this protocol consider details reported by Allaz (2017). The electron beam was set at 20 kV acceleration voltage, 100 nA beam current, and 5 µm beam diameter. For analyses of monazite < 10 µm in diameter, the beam diameter was set to 3 µm. The Mα1 lines of Th and Pb and the Mβ1 lines for U of a PETH crystal in a spectrometer with a capsuled Xe proportional counter were selected for monazite analysis. Calibration of Pb was carried out on a natural crocoite. The U and Th were calibrated on metal reference materials. For calibration of REE with the exception of La, which was only available from the Smithsonian Institution (Jarosewich and Boatner 1991), an alternative set of Pb-free REE-ultra-phosphates from ASTIMEX Ltd. was used as reference materials. More details of the analytical protocol are reported in the Online Resource 1 and Online Resource 2. The measured data for REE were corrected offline for mutual interferences using an Excel-based spreadsheet in a similar way as is explained in Osbahr et al. (2015). Subsequently the instrument drift was corrected for P, La, Ce, Nd, Sm and Y measuring a monazite reference material from ASTIMEX Ltd. (natural crystal from Buenopolis, Brazil) as unknown every 24 h. The instrument drift was assumed to be linear over time. Analyses with measurable contents of Al were omitted from the dataset as well as analyses with totals outside the range from 98.0 to 101.5 wt%.

A reference monazite labelled as Madmon, with validated special ThO_2*-PbO characteristics (Schulz and Schüssler 2013) was used for offline re-calibration of ThO_2, as well as for the control of data by repeated measurements at the beginning, midterm and end of analytical sessions. Interference of YLγ on the PbMα line was corrected by linear extrapolation of correction factors gained from analysis of various Y-bearing standards, as proposed by Montel et al. (1996). An interference of ThMγ on UMβ was also corrected. The number of single analyses varies with the grain size of the monazites, e.g. 1–2 analyses in grains of < 40 µm and up to 10 analyses in grains of 100 µm in diameter. Monazite ages were first calculated from each single analysis using the method of Montel et al. (1996). A 1σ error deduced from the counting statistics (JEOL error) and an error $\varepsilon_{Pb} = \sqrt{(Cts/s_{PEAK} + Cts/s_{BKG})}/(Cts/s_{PEAK} - Cts/s_{BKG})$ was propagated to an error in Pb element %. For Pb the error in element % is ~ 0.004 (recalculated from the JEOL error), or ~ 0.001 (recalculated from ε_{Pb}) for the reference monazite Madmon (~ 0.25 wt% Pb). We applied an error in Pb element % of

0.003 to all analyses, which propagates for the reference monazite Madmon with ~ 506 Ma typically to ± 12 Ma (2σ), and for Carboniferous monazites (~ 0.085 wt% Pb) to 20–30 Ma (2σ). In a second step, monazite ages were further determined using the ThO_2*–PbO isochrone method (CHIME) of Suzuki et al. (1994) where ThO_2* is the sum of the measured ThO_2 plus ThO_2 equivalent to the measured UO_2. This age is based on the slope of a regression line in ThO_2* vs PbO coordinates forced through zero. As the calculation of the regression line provides underestimation of the error, in a third step the weighted average ages for monazite populations were calculated from the single analyses defining the regression line using Isoplot 3.0 (Ludwig 2001). Weighted average ages were also calculated from the ages of single analyses when a large monazite allowed several analyses, and from clusters composed of many small monazites. As the sizes of most monazite grains are below 50 μm (Table 1), it was intended to perform a narrow grid of full quantitative analyses. In all analysed samples, the isochrone ages and the weighted average ages coincide within the error. The age data are interpreted as the time of closure for the Th–U–Pb system of monazite during growth or recrystallization in the course of metamorphism.

5 Monazite ages and mineral chemistry

In the garnet micaschists the monazite appears in different grain sizes and microstructural associations (Fig. 3). Grains with an elongated shape and an average length of 200 μm and width of 50–150 μm allowed for up to 15 single spot analyses (Fig. 3a, b). The grains are parallel to S_2 foliation. Single grain weighted average ages of such large grains in sample RZ42 are between 326 ± 9 and 312 ± 12 Ma. There are also large monazites with more embayed grain boundaries (Fig. 3c). In large monazite, darker cores and lighter rim zones with higher ThO_2 contents are observed in the BSE image. In samples RZ29, RZ31 and RZ33 one observes large monazite with weighted average ages between 351 ± 15 and 320 ± 15 Ma. Monazite displays successive stages of a double corona formation. In an early stage, the monzite is rimmed by allanite with only single tiny apatite grains in between (Fig. 3d). In the more progressed stages, the apatite corona increases while the monazite size decreases by consumption or decomposition (Fig. 3e). At the late stage of double corona formation, only elongated thin relics of monazite remain within the apatite zone. The allanite mantle is composed of crystals with radial orientation (Fig. 3f). The relative amount of this monazite involved in such corona structures can be estimated from the monazite ternary locking (Table 1). In sample RZ29 > 30% of monazite is locked by allanite and epidote, whereas the predominant large monazites in sample RZ42 are mainly locked in biotite.

Other microstructural features are clusters composed of numerous small monazite grains with diameters of mostly < 10 μm (Fig. 3g, h). These small monazite grains are partly surrounded by allanite. Cluster monazites dominate in sample RZ31, where REM-MLA recorded much more grains with smaller MD50 diameter (grain size at 50 wt% of cumulative grain size distribution), when compared to the other samples (Table 1). The cluster monazite in association with allanite, plagioclase and mica display also Carboniferous ages of 313 ± 8 to 304 ± 6 Ma, with a tendency to younger ages. The monazite clusters mostly take place in large mica (Fig. 3g), but can also found in plagioclase (Fig. 3h). The diverse distribution of these monazite microstructures among the samples are reflected by the number of single grains, the area of the grains and the grain size distribution, as indicated by the MD50 value of the cumulative grain size distribution curve (Table 1). The cluster microstructure in sample RZ31 is reflected by 292 monazite grains at a MD50 of 30 μm (Table 1). Accordingly the samples RZ42 and RZ29 have few, but large monazite grains. Large monazites dominate in sample RZ42 with an MD50 of 95 μm (Table 1).

The monazites in the three studied samples display a diverse mineral chemistry (Table 2; Online Resource 3). In the age vs Y_2O_3 plot, monazites in sample RZ29 are uniformly high in Y_2O_3 (~ 2 wt%). In samples RZ31 and RZ42 dominate monazites low in Y_2O_3 (0.4 wt%), but also some higher Y_2O_3 contents up to 2 wt% are observed (Fig. 4a). Sample RZ33 displays comparable broad variation in monazite Y_2O_3 contents. In the UO_2 vs age distribution, monazite of all samples concentrate around 0.8 wt% (Fig. 4b). Samples RZ31 and RZ33 display a large spread in the monazite *X*HREE + Y vs *X*LREE diagram (Fig. 4c). In contrast, monazite in sample RZ29 have higher *X*HREE + Y than in sample RZ42. In *X*$GdPO_4$ vs *X*YPO_4 coordinates, the monazites slightly exceed the limit of the garnet zone or garnet isograd as given by Pyle et al. (2001), but do not reach the limit toward the sillimanite zone at 0.06 *X*YPO_4 and migmatism at 0.08 *X*PO_4 (Fig. 4d). The dominant cheralite exchange (Th or U + Ca = 2 REE) is typical for systems with elevated Ca in bulk rock composition (Spear and Pyle 2002). Many monazites in samples RZ29 and RZ31 display a tendency toward higher Ca and deviate from the cheralite substitution trend (Fig. 4e). Low concentrations of HREE can be expected in monazite, however, the HREE vs LREE fractionation, represented by Gd_N/Yb_N and Ce_N/Gd_N coordinates, is given in Fig. 4f. The Eu has not been considered, as many monazites have no or negligeable Eu. The LREE fractionation in each of the samples RZ29, RZ33 and RZ42 is quite uniform, but the variation between the samples is

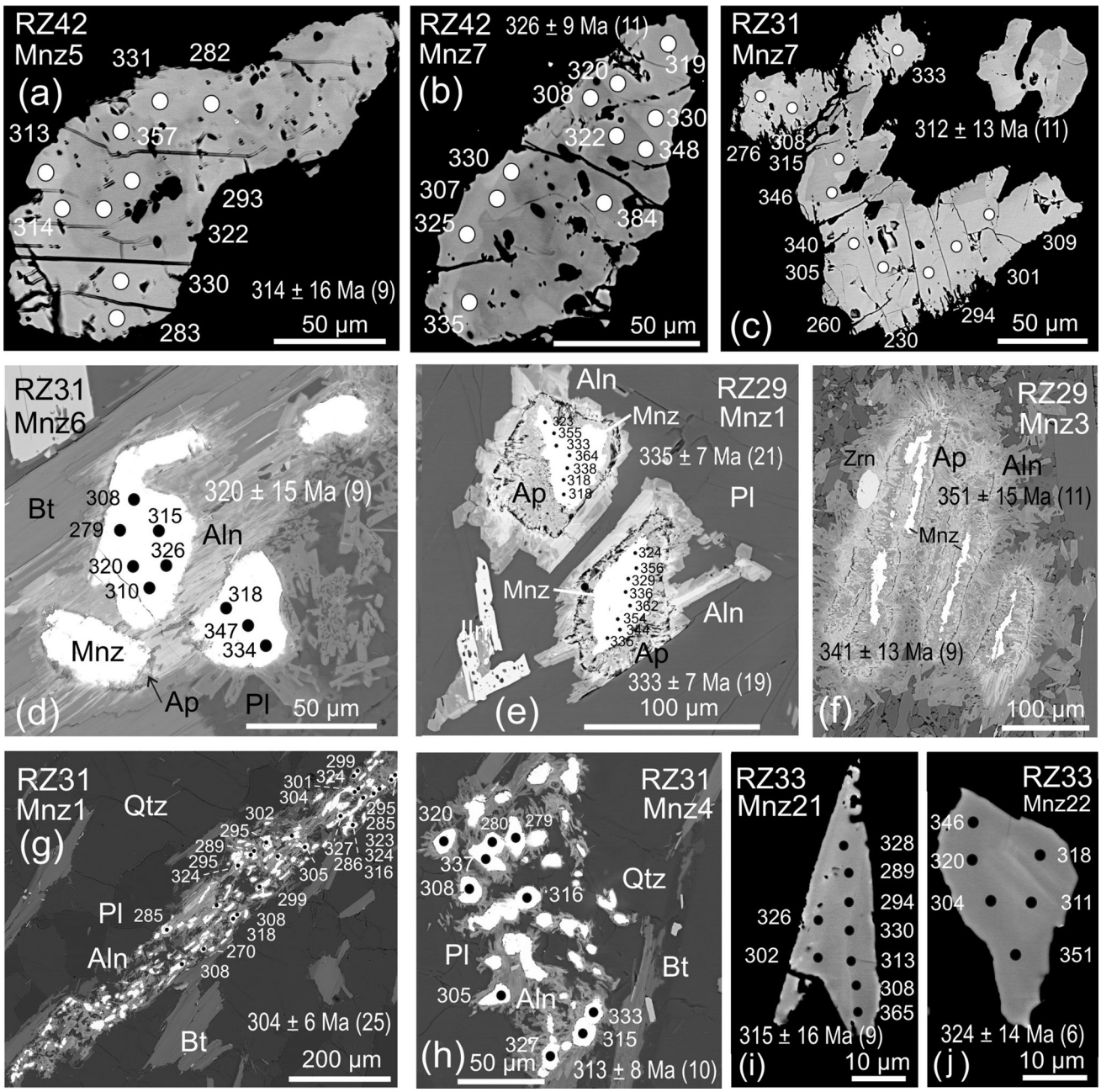

Fig. 3 Microstructures of monazite in backscattered electron images (BSE). Numbers are single Th-U–Pb ages in Ma. Weighted averages with 2σ error are calculated from several analyses within a grain, and from several small grains analysed by a single measurement. **a** Large monazite (Mnz) with slightly embayed rims and patchy darker core zones, with Carboniferous ages. **b** Large monazite with patchy darker core zone. **c** Embayed large monazite with darker domains. **d** Carboniferous monazite in biotite (Bt) with tiny apatite (Ap) at the rim and formation of allanite (Aln), initial stage of corona structure. **e** Progressed stage of corona formation with broad apatite zones. Only some single ages are labelled for spread of data. **f** Late stage of corona formation with broad apatite and allanite rims and thin relic monazite. Sutured monazite grain boundaries signal dissolution. Compared to **e**, the relic monazite cores are older. **g** Large cluster of small monazite grains which are surrounded by allanite and biotite. **h** Details of monazite cluster arrangement in plagioclase (Pl), quartz (Qtz) and biotite (Bt), with allanite rims around all small monazite grains. (**i**, **j**) Small Carboniferous monazite surrounded by allanite coronas (not visible due to BSE contrast/brightness); with stable grain boundaries and no signs of possible fluid-mediated marginal dissolution-repricipitation

considerable, with sample RZ29 in an intermediate position. In contrast, monazite in sample RZ31 displays a considerable variation in the LREE, with a distinct population at low Gd_N/Yb_N, belonging to a single large, 312 ± 18 Ma old grain (Fig. 4f). This may be an effect of the abundant cluster monazite microstructures.

Table 2 Selected electron microprobe analyses of metamorphic monazite from metapelites of the Schrankogel complex in the Oetztal-Stubai basement, Alpeiner Valley around Franz-Senn-Hütte

Comment	P_2O_5	La_2O_3	Ce_2O_3	Pr_2O_3	Nd_2O_3	Sm_2O_3	Eu_2O_3	Gd_2O_3	Y_2O_3	HREE	SiO_2	CaO	ThO_2	UO_2	PbO	Total	Th_{Suz}	ThO_2*	Age	±2σ
RZ29-Mnz1-3	30.08	12.89	28.11	2.86	12.11	2.02	0.38	1.67	1.756	1.204	0.131	1.304	3.75	1.064	0.094	99.43	6.343	7.207	308	21
RZ29-Mnz1-5	30.04	12.95	27.85	2.80	12.01	1.96	0.36	1.50	1.737	1.156	0.182	1.479	3.96	0.959	0.099	99.05	6.230	7.080	331	22
RZ29-Mnz1-7	29.75	12.66	28.37	2.86	12.55	2.12	0.41	1.60	1.802	1.137	0.161	1.175	3.16	0.975	0.089	98.82	5.568	6.326	333	24
RZ29-Mnz1-8	30.32	12.75	28.31	2.90	12.51	2.08	0.38	1.58	1.803	1.171	0.158	1.137	3.46	0.904	0.088	99.55	5.633	6.401	325	24
RZ29-Mnz1-9	29.79	13.32	28.58	2.89	11.95	1.96	0.33	1.52	1.630	1.129	0.122	1.196	3.37	0.910	0.095	98.81	5.579	6.339	353	24
RZ29-Mnz1-20	30.34	13.06	28.33	2.89	12.13	2.02	0.36	1.51	1.788	1.125	0.162	1.346	3.23	0.884	0.085	99.27	5.374	6.106	329	25
RZ29-Mnz3-7	30.16	12.71	28.03	2.90	12.34	1.99	0.35	1.64	1.926	1.187	0.164	1.599	3.47	0.838	0.091	99.39	5.455	6.198	349	25
RZ29-Mnz3-8	30.19	13.90	28.73	2.83	11.62	1.90	0.31	1.38	1.752	1.214	0.149	1.640	2.91	0.737	0.080	99.33	4.670	5.307	359	29
RZ29-Mnz3-9	30.14	12.86	27.86	2.87	11.96	2.04	0.36	1.54	1.983	1.216	0.192	1.713	3.61	0.868	0.089	99.32	5.662	6.435	330	24
RZ29-Mnz5-2	29.70	13.73	28.25	2.78	11.71	1.85	0.33	1.28	1.390	0.899	0.264	2.291	3.14	0.664	0.068	98.35	4.664	5.300	304	29
RZ31-Mnz1-5	29.82	13.68	30.14	2.88	12.48	2.14	0.25	1.75	0.180	0.361	0.447	0.981	3.80	0.682	0.076	99.66	5.287	6.009	299	25
RZ31-Mnz1-8	29.69	14.29	30.68	2.87	12.11	1.85	0.26	1.09	0.092	0.205	0.399	1.160	3.99	0.646	0.078	99.41	5.353	6.085	304	25
RZ31-Mnz4-6	30.04	13.58	30.05	2.92	12.47	2.00	0.27	1.46	0.784	0.649	0.284	0.980	3.14	0.827	0.076	99.51	5.128	5.827	308	26
RZ31-Mnz4-9	30.20	12.94	29.40	2.90	12.34	2.07	0.35	1.59	1.030	0.787	0.216	1.105	3.26	1.007	0.092	99.29	5.753	6.536	333	23
RZ31-Mnz5-10	29.78	13.21	29.78	2.91	12.67	2.14	0.39	1.66	0.465	0.680	0.185	1.097	3.11	0.925	0.078	99.07	5.377	6.109	302	25
RZ31-Mnz5-11	29.71	14.01	30.02	2.84	12.23	1.96	0.32	1.39	0.254	0.482	0.182	1.355	3.35	0.953	0.093	99.14	5.675	6.448	342	24
RZ31-Mnz6-6	30.07	13.35	30.39	3.02	13.00	2.11	0.36	1.58	0.426	0.495	0.166	0.900	2.85	0.710	0.067	99.48	4.533	5.151	310	30
RZ31-Mnz6-9	29.99	12.64	28.37	2.85	12.03	2.10	0.44	2.07	1.347	1.008	0.183	1.168	3.80	0.975	0.098	99.08	6.136	6.973	334	22
RZ31-Mnz7-3	29.66	13.65	30.49	3.02	12.57	1.88	0.30	1.17	0.154	0.251	0.201	1.080	3.68	0.919	0.087	99.10	5.860	6.659	308	23
RZ31-Mnz7-7	29.56	13.75	30.67	2.94	12.43	1.91	0.33	1.21	0.169	0.280	0.191	1.128	3.49	0.980	0.086	99.13	5.874	6.674	305	23
RZ33-Mnz1-5	30.30	12.72	28.95	3.31	14.85	2.76	0.47	1.79	0.588	0.651	0.119	0.819	2.23	0.629	0.057	100.25	3.761	4.274	314	36
RZ33-Mnz2-4	30.33	11.84	27.26	2.99	13.63	2.54	0.51	2.51	1.626	1.341	0.173	0.938	3.16	0.682	0.074	99.61	4.729	5.374	325	28
RZ33-Mnz3-2	29.83	12.44	28.52	3.22	14.52	2.58	0.46	1.90	0.814	0.688	0.113	0.887	2.46	0.630	0.063	99.13	3.966	4.506	330	34
RZ33-Mnz20-2	30.26	12.87	28.43	3.14	13.77	2.46	0.45	2.04	1.262	1.141	0.154	0.761	2.33	0.493	0.056	99.63	3.464	3.936	339	39
RZ33-Mnz20-3	30.32	12.87	29.04	3.18	14.15	2.42	0.49	2.02	1.236	1.049	0.085	0.552	1.32	0.412	0.034	99.18	2.342	2.661	305	58
RZ33-Mnz20-13	30.02	12.03	27.01	3.01	13.84	2.52	0.42	2.31	1.426	1.201	0.132	1.075	3.47	0.571	0.075	99.12	4.689	5.330	332	29
RZ33-Mnz20-14	29.89	12.16	27.31	3.07	13.79	2.46	0.41	2.16	1.317	1.118	0.127	1.002	3.41	0.549	0.079	98.86	4.574	5.200	359	29
RZ33-Mnz21-7	30.14	12.39	28.39	3.19	14.08	2.53	0.44	2.02	1.234	1.129	0.121	0.735	2.08	0.729	0.059	99.27	3.916	4.448	313	34
RZ33-Mnz21-8	29.95	12.34	28.19	3.19	14.32	2.53	0.49	2.09	1.291	1.030	0.128	0.815	2.13	0.728	0.058	99.27	3.957	4.495	308	34
RZ33-Mnz22-3	29.71	12.87	29.13	3.26	14.57	2.47	0.37	1.74	0.678	0.701	0.164	0.712	2.39	0.548	0.056	99.38	3.670	4.171	320	37
RZ42-Mnz2-7	29.69	14.01	30.33	3.04	12.70	2.04	0.27	1.23	0.161	0.342	0.251	0.860	3.82	0.579	0.075	99.41	5.015	5.701	313	27
RZ42-Mnz2-13	29.98	14.33	30.21	2.88	12.27	1.88	0.26	1.21	0.255	0.379	0.243	0.892	3.93	0.710	0.080	99.52	5.485	6.235	305	25
RZ42-Mnz5-6	29.61	13.79	30.10	3.01	12.76	2.03	0.25	1.28	0.339	0.436	0.207	0.826	3.83	0.524	0.073	99.06	4.863	5.529	314	28
RZ42-Mnz5-10	29.65	13.87	29.93	2.94	12.25	1.98	0.33	1.22	0.270	0.382	0.283	0.961	4.27	0.706	0.078	99.12	5.771	6.560	283	23
RZ42-Mnz6-2	30.11	13.88	29.53	2.88	12.32	2.04	0.24	1.51	0.635	0.715	0.197	0.895	3.75	0.423	0.074	99.19	4.506	5.123	343	30

Table 2 (continued)

Comment	P_2O_5	La_2O_3	Ce_2O_3	Pr_2O_3	Nd_2O_3	Sm_2O_3	Eu_2O_3	Gd_2O_3	Y_2O_3	HREE	SiO_2	CaO	ThO_2	UO_2	PbO	Total	Th_{Suz}	ThO_2*	Age	±2σ
RZ42-Mnz7-1	29.68	14.32	30.22	2.88	12.30	1.94	0.26	1.25	0.283	0.421	0.255	1.057	3.86	0.586	0.078	99.38	5.072	5.766	319	27
RZ42-Mnz7-4	29.68	14.68	30.39	2.88	11.88	1.82	0.28	1.14	0.356	0.456	0.225	0.876	3.79	0.599	0.080	99.13	5.047	5.737	330	27
RZ42-Mnz7-9	30.18	17.20	31.10	2.59	10.66	1.55	0.28	1.09	0.751	0.713	0.130	0.580	2.43	0.214	0.051	99.53	2.754	3.131	384	49
RZ42-Mnz7-10	29.68	12.81	28.13	2.80	12.19	2.28	0.37	2.39	1.438	1.293	0.104	0.987	3.32	0.837	0.083	98.71	5.314	6.039	325	25
35 Madmon	25.29	7.65	25.54	3.54	14.72	3.65	0.00	1.98	0.879	0.478	2.886	0.129	10.89	0.460	0.266	98.35	10.906	12.405	505	12

Data are given in wt%. ThO_2* is calculated from Th and U after Suzuki et al. (1994). Monazite ages from single analyses are given with 2σ error, see text. *Mnz* monazite single grain; data from reference standard monazite Madmon (Schulz and Schüssler 2013) is weighted average of 20 single analyses performed during the sessions on the samples. The monazites were analysed with a JEOL JXA-8530F at Helmholtz Institute Freiberg of Resource Technology. The analytical protocol and a complete monazite data set are reported in Online Resource 1, Online Resource 2 and Online Resource 3

In the ThO_2*–PbO diagrams, isochrones with Carboniferous ages prevail (Fig. 5). The isochrones are sometimes characterised by low values of R^2 and weak MSWD, as it appears typical for metamorphic monazites. Sample RZ29 with many corona structures displays an isochrone at 335 ± 4 Ma (Fig. 5a). The weighted average calculation from the single monazites defining an isochrone results in a considerable reduction of error. Also in the monazite relics within corona structures, the corresponding ages are observed (Fig. 3e, f). In the samples RZ31 and RZ33 monazites defining isochrones at 319 ± 4 Ma and 320 ± 4 Ma prevail, beside minor populations showing Permian isochrones at 284 ± 6 and 276 ± 7 Ma (Fig. 5b, c). Apparently, the cluster monazites are somewhat younger as the overall isochrone (Fig. 3g, h). In sample RZ42 with many large monazite grains, most monazite analyses belong to the 319 ± 3 Ma isochrone (Fig. 5d). However, the weighted average ages from single large monazites can be younger (Fig. 3a, c). One can figure out a population of single monazite analyses which are distributed among several grains (Fig. 3a, b) which are arranged around isochrones at 356 ± 12 Ma and 357 ± 8 Ma in samples RZ33 and RZ42 (Fig. 5c, d). There is no distinct tendency between the bulk rock Ca and Al contents from calculated assay and the monazite ages given by the isochrones.

In the histogram view there are unimodal distributions around the Carboniferous isochrone ages (Fig. 6a–d). In sample RZ29, the older isochrone at 335 ± 4 Ma compared to the other samples is clearly matched by the maximum of the age distribution. The tendency toward Permian age monazites in samples RZ31 and RZ33 is matched by sub-maxima in the lower age flanks of the age distributions (Fig. 6b, c). In contrast, in sample RZ42 appears a sub-maximum at the higher age flank of the distribution which reflects the isochrone at 357 ± 8 Ma (Fig. 6d).

6 Mineral chemistry and geothermobarometry

6.1 Metapelites

The garnet- and staurolite-bearing micaschists (RZ33 and RZ42) show an overall mineral assemblage of garnet, kyanite, staurolite, biotite, muscovite, plagioclase and quartz (Table 1). Sample RZ42 is an aluminous gneiss and contains all three Al_2SiO_5-phases, as it also has been described by Purtscheller (1978) from other parts of the OSC. The aluminosilicates are not in invariant equilibrium, as andalusite statically overgrows the foliated fabric with kyanite and sillimanite. Garnet is variable in shape and

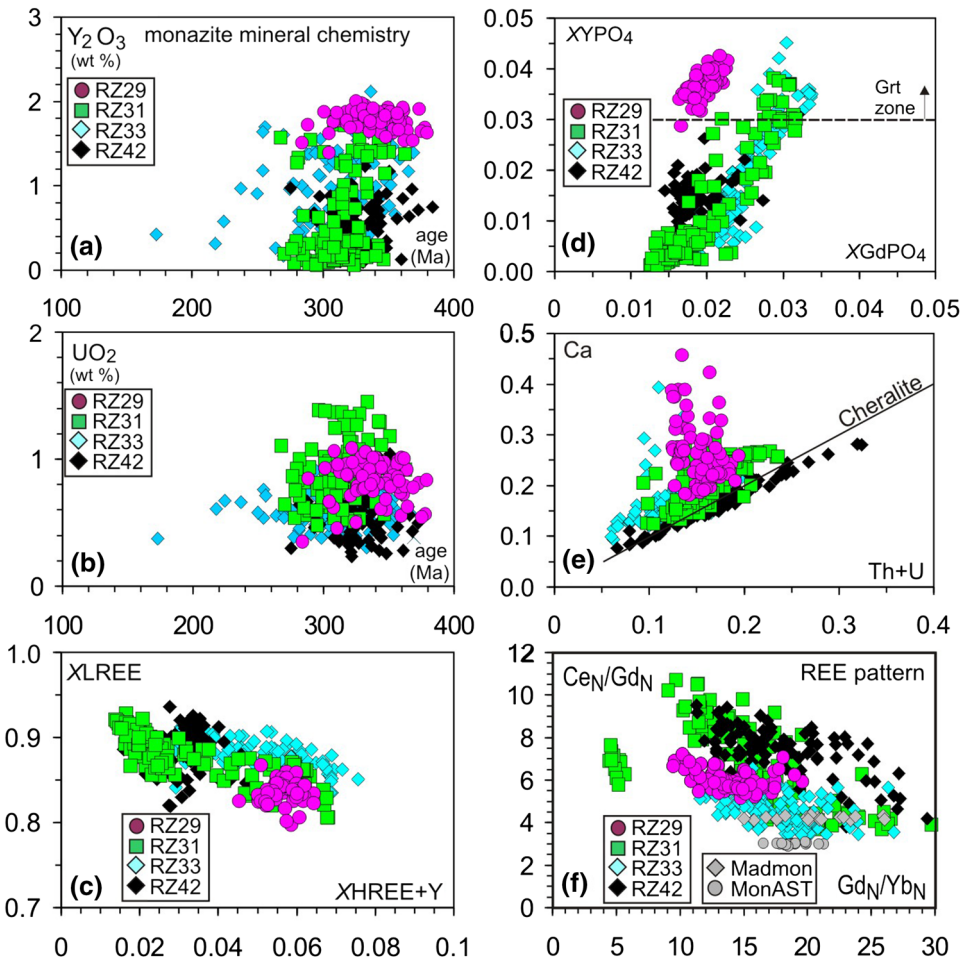

Fig. 4 Mineral chemistry of monazite and distributions of monazite Th–U–Pb chemical ages. **a** Monazite Y_2O_3 vs age. Note position of sample RZ29. **b** Monazite UO_2 vs age. **c** Monazite LREE and HREE compositions in mole fractions, with only negligeable variations in sample RZ29. **d** Diagram XGdPO$_4$ vs XYPO$_4$, with compositions above the garnet (Grt) metamorphic mineral zone as defined by Pyle et al. (2001). Moles calculated according to Pyle et al. (2001). **e** Monazite compositions in reference to the cheralite substitution trend. Note different trends in sample RZ29 compared to the other samples. **f** Normalised REE variation pattern in metamorphic monazite from Stubai micaschists, with HREE fractionation expressed as Gd_N/Yb_N versus LREE fractionation expressed as Gd_N/Yb_N. Note REE fractionation in pegmatitic reference monazites Madmon and MonAST

size. Crystals range from small (1 mm) isometric to several mm large subhedral to euhedral grains (Fig. 7a). Inclusions of quartz, ilmenite, titanite, mica and plagioclase line up and can be interpreted as relics of an internal foliation S_1i. Garnet zonations show a core-to-rim trend with decreasing spessartine (Sps 15–1 mol%, calculated from mole fraction × 100), grossular (Grs 20–10 mol%), and increasing pyrope with Prp 5–20 mol %. Some garnets display retrogressive spessartine-rich overgrowths. Such rim zones are characterised by decrease of the pyrope component (Fig. 7b, c). In sample RZ33 a large garnet porphyroblast displays the complete core-to-rim zonation profile (Grt-A). In sample RZ42 one garnet displays a zonation from the spessartine- and grossular-rich core with low pyrope, to a rim with intermediate compositions (Fig. 7c, Grt-B). Another garnet porphyroblast recorded these intermediate compositions in its core and displays the pyrope-rich and spessartine- and grossular-poor compositions in the inner rim (Fig. 7c, Grt-C). In consequence, the complete garnet mineral-chemical evolution can be deduced by a combination of both porphyroblast Grt-B and Grt-C zonation profiles (Fig. 7d). This appears when garnet porphyroblasts are not truncated in their cores, or are partly resorbed along their rims. The Ca-content in the RZ33 garnet core (XCa = 0.20) is considerably higher as in the RZ42 garnet cores with XCa = 0.1 (Fig. 7d). Such systematic differences in garnet XCa are related to the bulk composition of the samples (Spear 1993). This is supported by the Ca bulk rock calculated assay of 2.04 wt% in sample RZ33, and 0.92 wt% in sample RZ42 (Table 1). The garnet zonations in the metapelite samples represent segments of a common mineral-chemical trend, as can be demonstrated in the XMg-XCa coordinates (Fig. 7d). The core-to-rim zonation trends of the garnets B and C in sample RZ42 (Fig. 7c, d) correspond to the zonation in the rim of garnet A in sample RZ33 (Fig. 7b, d). From the decreasing spessartine (Mn) contents from cores to inner rims, it is clear that garnets A, B and C represent the same porphyroblast generation which crystallized during the same metamorphic event. It has been demonstrated from other polymetamorphic basement areas that garnet generations which crystallized during distinct thermal events (e.g. Carboniferous-Permian and Cretaceous) can be distinguished by their Mn zonation characteristics (Frank et al. 1987; Schulz 2014; 2017). The

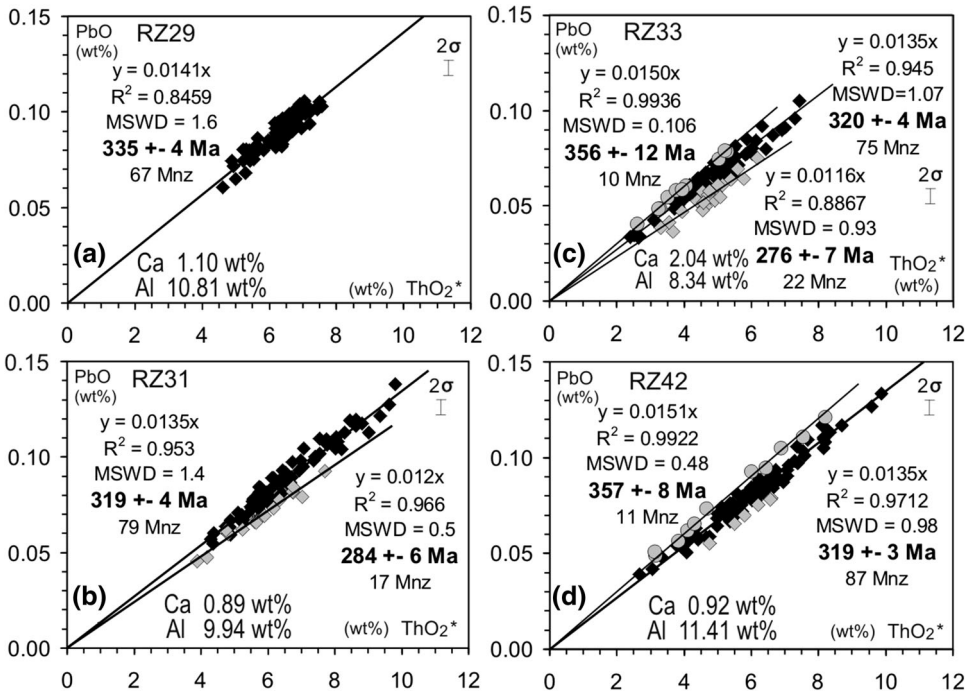

Fig. 5 Th–U–Pb chemical model ages of monazite (Mnz). Total ThO_2* vs PbO (wt%) isochrons diagrams. ThO_2* is $ThO_2 + UO_2$ equivalents expressed as ThO_2. General minimal 2σ error on monazite PbO analysis is shown by a bar. Regression lines with the coefficient of determination R^2 are forced through zero (Suzuki et al. 1994; Montel et al. 1996). Weighted average ages in Ma with MSWD and minimal error of 2σ are calculated from the single analyses belonging to an isochrone according to Ludwig (2001). The symbols mark analyses belonging to monazite age populations and defining isochrones, falling into Carboniferous, and Permian ranges of ages. Al and Ca are bulk rock compositions in wt% from Table 1

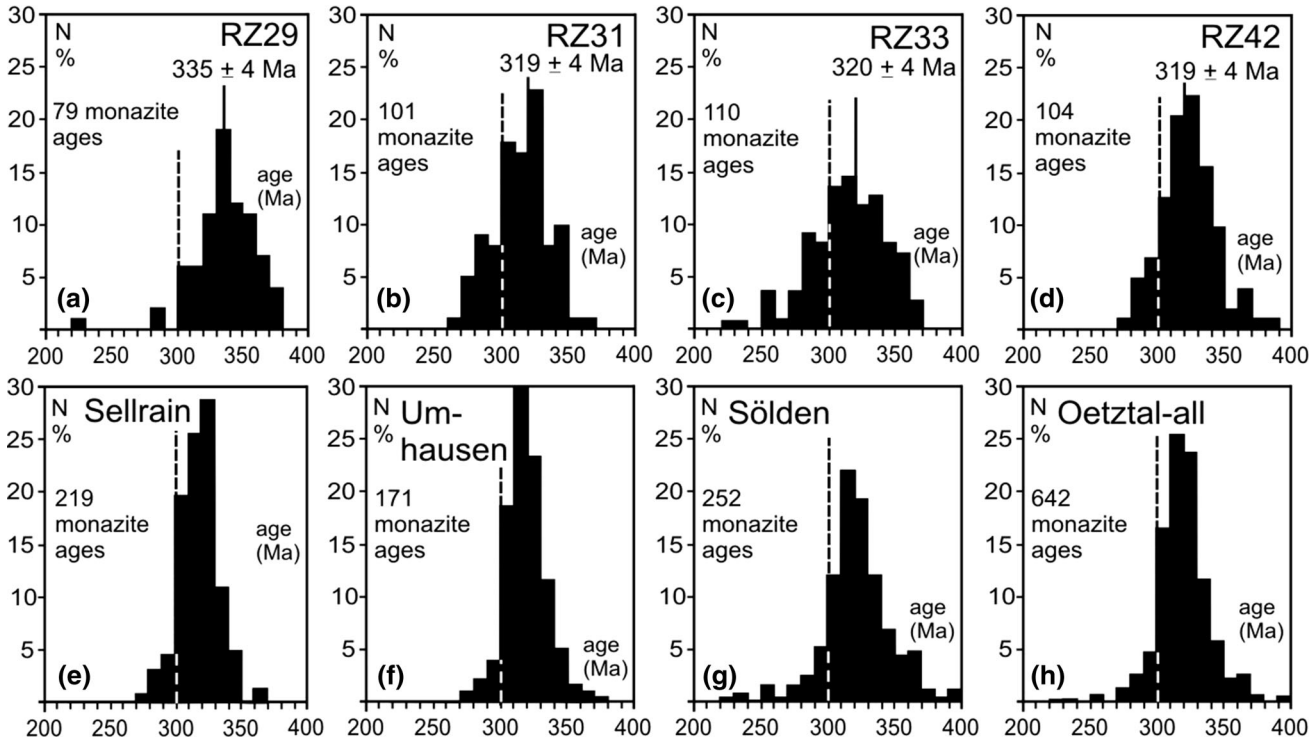

Fig. 6 Frequency distribution of the EMP-Th-U–Pb monazite ages. **a–d** Histograms of monazite ages in the Stubai samples, recalculated to percent. The weighted average isochrone ages from Fig. 4 are marked apart a 300 Ma reference line. **e–g** Histograms of monazite ages as reported by Rode et al. (2012) from regions in the Oetztal basement, recalculated to percent. **h** Histogram with summary of the monazite ages in (**e–g**)

preserved Mn zonation profiles signal that a possible post-crystalline diffusion at high temperatures was not significant. The increase of Mn in some tiny rim zones is related to retrogression, as it is accompanied by significantly decreasing Mg and Fe. Accordingly, the garnets in samples RZ33 and RZ42 with comparable high Mn in the cores

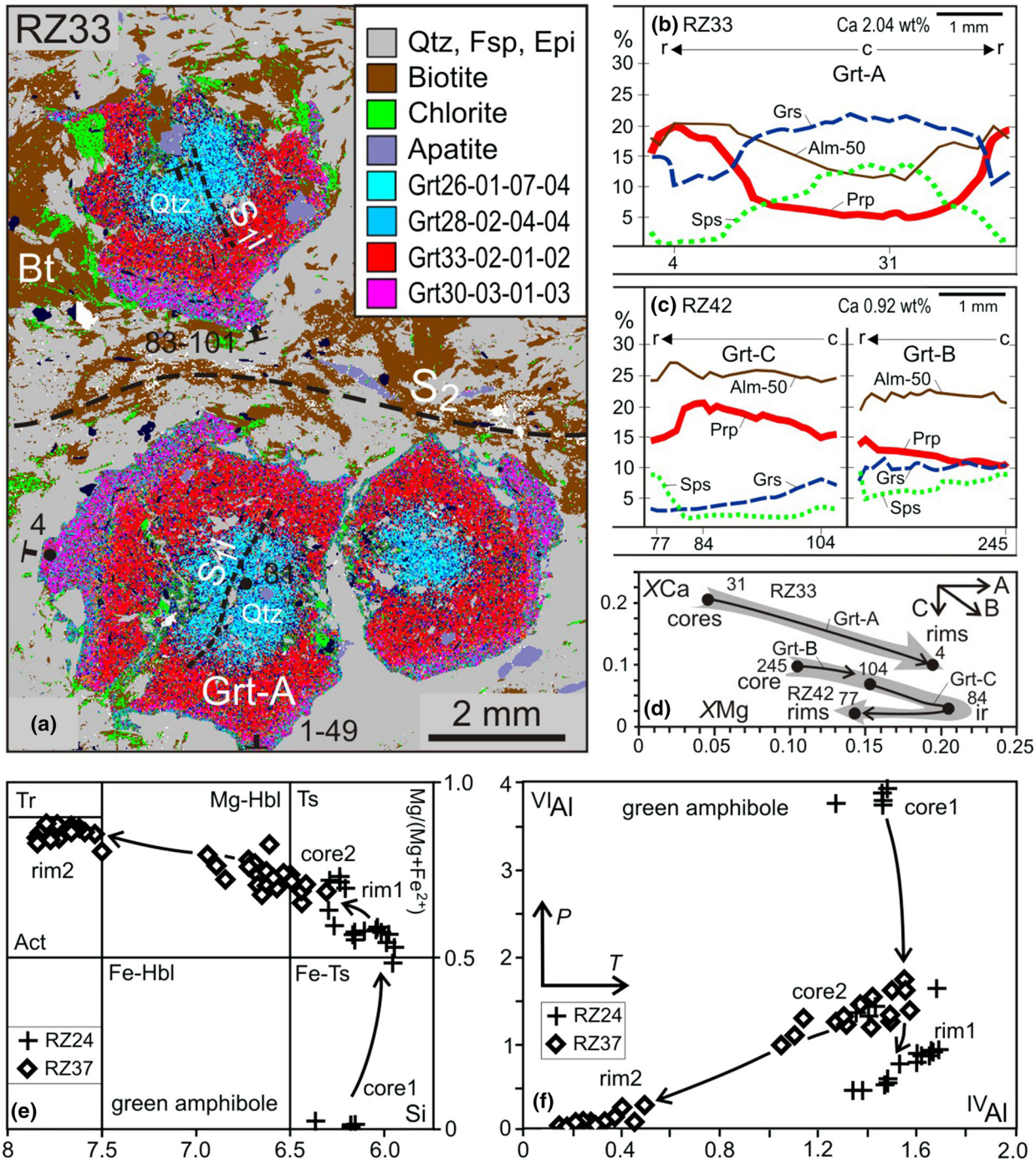

Fig. 7 **a** Map of energy dispersive X-ray (EDX) spectra in garnet micaschist. Spectra for garnet porphyroblasts are labelled in a generic way by Fe, Mg, Mn, and Ca contents in normalised element wt%. *Bt* biotite, *Grt* garnet. Locations of analytical profiles and traces of foliations S_1i by aligned elongated quartz (Qtz) inclusions and opaques, and S_2 by mica plates are marked. Numbers are EMP analyses along profiles. **b**, **c** Zonations in micaschist garnet including almandine (Alm-50%, due to scale), pyrope (Prp), grossular (Grs) and spessartine (Sps) components (in mole%). Numbers are selected garnet analyses used for geothermobarometry. The profiles are labelled from the cores (c) to the rims (r) of garnet. **d** Garnet zonations in *X*Mg-*X*Ca coordinates. Arrows indicate core-to-rim (c, r) zonation trends from single garnet profiles. Numbers are selected garnet analyses for geothermobarometry. Note different Ca bulk rock compositions in wt% from Table 1. The garnet *X*Mg-*X*Ca zonations refer to the semiquantitative pressure–temperature trends A (heating-compression), B (heating-decompression) and C (isothermal decompression), as outlined in Spear (1993). **e** Mineral chemistry and zonations of Ca-amphibole in metabasite samples, nomenclature according to Leake et al. (1997). **f** Ca-amphibole zonations in ^{IV}Al vs ^{VI}Al coordinates, with relative P–T trend. *c1, c2* cores, *r1, r2* rims of amphiboles

represent the first or early part of a single porphyroblast generation. Zoned garnets with lower Mn in their cores then can be explained by truncation beside the true core and/or crystallization at a later stage of the same porphyroblast generation.

Staurolite within the matrix is not zoned and chemically homogeneous with $Fe_{tot}/(Fe_{tot} + Mg)$ ratio of 0.87 to 0.91 and 11.7 to 13.4 wt% FeO. Staurolite inclusions in garnet are within the same compositional range. Biotite defines together with muscovite the main foliation S_2. Single biotites are not zoned. Depending on the sample, they display only little differences in composition with an overall range of *X*Mg between 0.42 and 0.47 (sample RZ42), and *X*Mg between 0.38 and 0.55 (sample RZ33). Among the microstructures, three different structural positions of biotite can be distinguished: (1) biotites aligned along the main foliation, (2) biotite as inclusions in garnet with evolving Ti-contents from 0.08 to 0.10 (p.f.u.), and (3) biotite in pressure shadows of garnets formed by the breakdown reaction of garnet = biotite + sillimanite + quartz. These biotites have highest Ti-contents (0.10–0.12 p.f.u). Matrix plagioclase shows a trend from An-rich (An_{30}) cores to albite-rich rims (An_{5-10}). Plagioclase grains within garnet (An_{25-30}) and in the pressure shadows (An_{10-20}) show lower An-contents. Aggregates with sericite are formed by breakdown reaction of staurolite and plagioclase during retrogression (Table 3).

Each garnet zonation trend in a single porphyroblast represents a segment in the overall P–T evolution. A crystallization of the garnets A, B, C first at increasing temperature and pressure, then during decompression at amphibolite facies conditions, followed by decompression-cooling can be semiquantitatively derived from the zonations in the *X*Mg-*X*Ca coordinates (Spear 1993). Cores of garnet and matrix plagioclase as well as relic mica and inclusion minerals in garnet may document the early stage of metamorphism. Late stage metamorphic evolution can be preserved in rims of garnet and matrix plagioclase, and large biotite in pressure shadows and microlithons. Thus, distinct single analyses of garnet which characterise the overall zonation trend in *X*Mg-*X*Ca coordinates were identified and selected (Fig. 7b–d). Plagioclase and biotite analyses from grains in corresponding microstructural positions (e.g. enclosed in garnet, aligned in S_2, in pressure shadows, in zoned plagioclase porphyroblasts, were chosen in each sample (Table 2). Accordingly, the garnet-biotite Fe–Mg exchange geothermometer (Bhattacharya et al. 1992; Holdaway 2001) and the garnet-plagioclase Ca-net-transfer geobarometers were applied. Pressures were calculated with the garnet-aluminosilicate-plagioclase-quartz (GASP) geobarometer involving kyanite, enclosing the internally consistent thermodynamic mineral data set (Holland and Powell 1998), with the activity models for garnet and plagioclase taken from Powell and Holland (1993) and Ganguly et al. (1996), and the corresponding updated calibrations by Wu et al. (2004) and Wu (2015).

Table 3 microprobe analyses (cations p.f.u.) of garnet (Grt), biotite (Bt), muscovite (Ms) and plagioclase (Pl) in micaschists and gneisses from the Schrankogel complex in the Austroalpine Oetztal-Stubai basement, Alpeiner Valley around Franz-Senn-Hütte, normalized to 12 oxygen (garnet), 11 oxygen (biotite, muscovite) and 8 oxygen (plagioclase). Almandine (Alm), anorthite (An), grossular (Grs), pyrope (Prp), spessartine (Sps) contents in mole%*100. Mineral analyses combined for geothermobarometric calculations are as follows: Sample RZ33: Grt31c–Bt119–Pl73; Grt4r–Bt108–Pl170/Pl73: Sample RZ42: Grt245c–Bt161–Ms187–Pl171; Grt104c–Bt161–Ms187–Pl171; Grt84r–Bt247–Ms187–Pl203; Grt77r–Bt247–Ms187–Pl203. *c* core, *r* rim

Grt	RZ33 31c	RZ33 4r	RZ42 245c	RZ42 104c	RZ42 84r	RZ42 77r
Si	3.013	2.972	2.997	3.004	3.003	3.000
Al	1.922	1.969	1.979	1.987	1.978	1.970
Fe	1.876	2.165	2.132	2.232	2.248	2.251
Mn	0.404	0.013	0.266	0.090	0.056	0.267
Mg	0.148	0.604	0.318	0.459	0.618	0.432
Ca	0.642	0.310	0.305	0.216	0.104	0.086
Tot	8.005	8.033	7.997	7.989	8.007	8.007
Alm	61.1	70.0	70.6	74.5	74.3	74.2
Prp	4.8	19.5	10.5	15.3	20.4	14.2
Sps	13.2	0.4	8.8	3.0	1.9	8.8
Grs	20.9	10.0	10.1	7.2	3.4	2.8
*X*Mg	0.048	0.195	0.105	0.153	0.204	0.142
*X*Ca	0.209	0.100	0.101	0.072	0.034	0.028
	Bt119	Bt108	Bt161	Ms187	Bt247	Ms187
Si	2.727	2.737	2.636	3.152	2.654	3.152
^{IV}Al	1.273	1.263	1.364	0.848	1.346	0.848
^{V}IAl	0.349	0.368	0.419	1.821	0.387	1.821
Ti	0.095	0.090	0.045	0.008	0.095	0.008
Fe	1.261	1.183	1.155	0.092	1.229	0.092
Mn	0.003	0.003	0.005	0.001	0.005	0.001
Mg	1.186	1.240	1.443	0.096	1.255	0.096
Ca	0.000	0.000	0.002	0.001	0.001	0.001
Na	0.024	0.028	0.027	0.131	0.030	0.131
K	0.922	0.919	0.692	0.839	0.793	0.839
Tot	7.840	7.831	7.787	6.990	7.796	6.890
XMg	0.48	0.51	0.56	0.51	0.51	0.49
Pl	73	76	171	173	203	204
Si	2.859	2.784	2.847	2.842	2.779	2.805
Al	1.129	1.203	1.150	1.152	1.220	1.190
Ca	0.153	0.226	0.152	0.163	0.222	0.205
Na	0.849	0.788	0.846	0.846	0.762	0.798
K	0.013	0.002	0.008	0.002	0.013	0.004
Tot	5.006	5.008	5.003	5.005	4.996	5.001
An	15.0	22.2	15.1	16.1	22.3	20.3

In detail, garnet cores started to crystallize at ~ 460–500 °C/7–8 kbar and maximal pressures of 12 kbar were reached at 680 °C (Fig. 8a). This was followed by a decompression to 6 kbar, accompanied by only slight cooling to 660 °C. The Mg-poor and Mn-enriched marginal zones of some garnets signal a cooling and decompression toward 600 °C and 4 kbar (Fig. 8a). Geothermobarometric estimates include a minimum error of ± 35 °C and ± 1 kbar (Spear 1993). Thus, resulting errors of thermobarometric calculations are much higher than quantitative systematic error in thermodynamic data and microprobe analysis. Considering this, the shape of the P–T path and/or ΔP/ΔT trends can be obtained. When applied to garnet cores and rims in the samples RZ33 and RZ42, the single P–T segments line up to a clockwise prograde-retrograde P–T path (Fig. 8a).

6.2 Metabasites

Two metabasite samples were selected for mineral chemistry analyses and related geothermobarometry (Online Resource 4). Sample RZ 24 is an amphibolitized eclogite. Garnets are up to 3 mm in diameter in a matrix composed of fine-grained symplectites, green amphiboles, plagioclase, epidote and quartz. Titanite and ilmenite appear as the Ti-bearing phases. From cores to rims the garnets are zoned with decreasing spessartine (Sps 12–1 mol%, calculated from mole fraction × 100), strongly increasing pyrope (Prp 5–25 mol %), at quite constant high grossular (Grs 22–25 mol %). This pyrope zonation trend indicates crystallization at increasing temperature. The Mg- and Ca-rich garnet rim compositions are typical of eclogites without coesite. In combination with the symplectites this indicates a former eclogitic stage for the Schrankogel complex. Many inclusions of epidote towards the garnet rim are typical. Plagioclase is slightly zoned, sometimes with oligoclase cores, but mostly with albitic compositions at An < 10. Plagioclase is also albitic in the symplectites with secondary clinopyroxene with Jd < 10. Ca-amphiboles in the metabasites display considerable zonations and compositional variations which can be described best in the Si vs *X*Mg nomenclature diagram (Fig. 7e) after Leake et al. (1997), and in ^{IV}Al vs. ^{VI}Al coordinates (Fig. 7f). Amphibole cores in sample RZ24 have high ^{VI}Al (~ 3.8 p.f.u.) of ferro-tschermakite and rims with lower ^{VI}Al (1.0) at similar ^{IV}Al (1.6). In sample RZ37 one observes amphibole cores with Mg-hornblende compositions at ^{VI}Al of 1.5 and ^{IV}Al of 1.2–1.6 (p.f.u.). In this sample, amphibole rims and also a second generation of porphyroblasts are actinolites with ^{VI}Al and ^{IV}Al below 0.4 (Fig. 7e, f). The garnet-clinopyroxene Fe–Mg geothermometer cannot be used for sample RZ24, as the only observed clinopyroxene in the symplectites has low Na (Jd < 10), and no

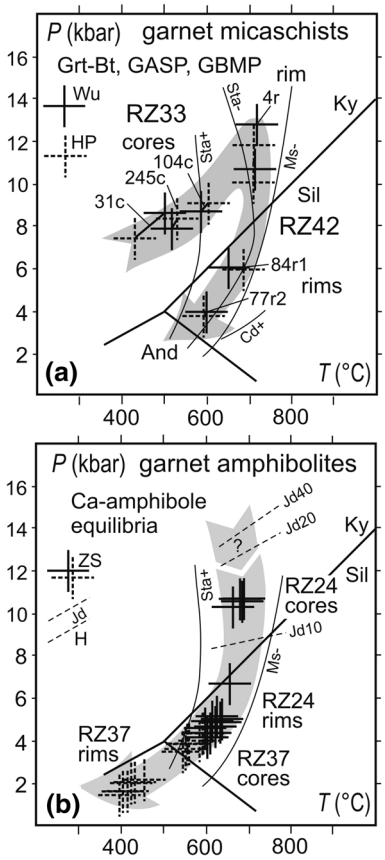

Fig. 8 **a** Geothermobarometry and P–T estimates from garnet micaschists. Crosses mark results from garnet-biotite (Grt-Bt) thermometers and GASP and GBMP barometers; HP—Holland and Powell (1998); Wu—Wu (2015). See text and Table 2 for details and combination of analyses. Arrow indicates P–T trend given by combination of data from samples RZ33 and RZ42. The aluminosilicates (And, Ky, Sill), cordierite-in (Cd +), muscovite-out (Ms −) and staurolite-in and -out (Sta +, Sta −) univariant lines are after Spear (1993). Bold crosses marks a general uncertainty of ± 50 °C and ± 1.0 kbar. **b** Geothermobarometry and P–T estimates (crosses) from amphibolitized eclogite (RZ24) and amphibolite (RZ37), by the Ca-amphibole equilibria geothermobarometer (ZS) by Zenk and Schulz (2004). Isopleths for jadeite (Jd10; Jd20; Jd40) content in clinopyroxene after (H) Holland (1980; 1983). A potential and questionable higher pressure stage indicated by decomposition of Na-rich clinopyroxene to symplectites is indicated

Na-rich clinopyroxene corresponding to the eclogitic stage and coexisting with the garnet remained preserved (Fig. 8b). However, a pressure estimation for the symplectitic stage is possible using the Jd-in-clinopyroxene barometer of Holland (1980; 1983).

The dependence of Si and ^{IV}Al on temperature and ^{VI}Al on pressure in Ca-amphiboles in assemblages with plagioclase, epidote, quartz, ilmenite and/or titanite can be used for P–T estimates. The amphibole-bearing assemblages in sample RZ24 and also in the amphibolite sample RZ37 match the requirements for the application of the geothermobarometer of Zenk and Schulz (2004), which

involves experimental data listed by Gerya et al. (1997). Accordingly, the zoned ferro-tschermakitic to tschermakitic amphiboles in sample RZ24 crystallized during a nearly isothermal decompression from 11 to 4 kbar at 650–600 °C (Fig. 8b). The Mg-hornblende and actinolites in sample RZ37 crystallized at mainly decreasing temperatures from 600 to 400 °C/4–2 kbar (Fig. 8b). The P–T estimates from the metabasites contribute with retrograde P–T segments to the overall clockwise P–T path of the Schrankogel complex.

7 Discussion

The combination of the thermobarometric results from garnet metapelites and metabasites in the Schrankogel complex points to a clockwise P–T path which evolved mainly in the pressure-dominated amphibolite-facies. A prograde P–T path started in the kyanite stability field. Maximal pressures and temperatures range around 12 kbar and 650 °C. Then the P–T path passed the sillimanite field at decreasing pressure. Zoned green amphiboles recorded conditions from 5 to 4 kbar/600 °C to 2 kbar/400 °C, indicating a retrograde P–T path which entered the andalusite stability field (Fig. 9a). This meets the observation of the three alumosilicates in sample RZ42, where andalusite overgrows the fabric at a late stage of the evolution. The amphibolite-facies metamorphism in the Alpeiner Valley matches the Variscan (Carboniferous) event as described from the Sellrain, Umhausen and Sölden areas, as reported in Rode et al. (2012). It was not possible to constrain high pressure eclogite facies P–T conditions in the Schrankogel complex metabasites, as it has been described from the Central Metabasite Zone (CMB) in the Oetztal by Miller and Thöni (1995). They reported minimum pressures for the CMB eclogites at ~ 15 kbar at 650–700 °C from the Jd-in-clinopyroxene barometer by Holland (1980). They also stated that their alternative estimates, based on phengite equilibria and thermodynamic data, at around 27 kbar, are afflicted by the assumption of a very low water activity, and are not confirmed by observation of coesite or relics of it. Omphacite with high jadeite contents was not preserved in the Schrankogel complex metabasites. However, the pervasive occurrence of symplectites with low jadeite bearing clinopyroxene demonstrates that the metabasites should have experienced somewhat higher pressures as were actually recorded by the green amphiboles (Fig. 8b).

By comparing similar P–T paths from various parts of the Oetztal and Stubai basement (Fig. 9a) to the age distribution pattern of monazite (Fig. 9b, c), one can argue that the monazite ages not necessarily coincide with the time of garnet growth. However, the P–T paths deduced

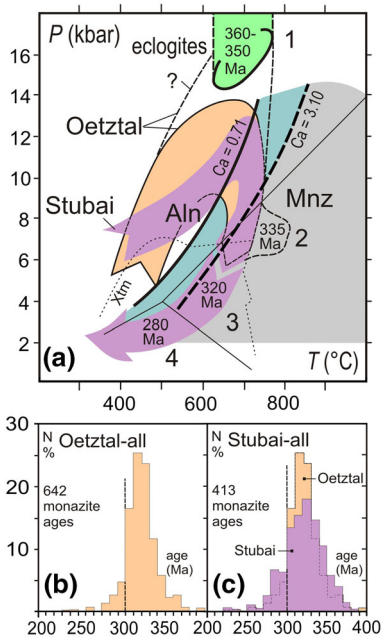

Fig. 9 **a** P–T-t evolution and monazite ages from the Schrankogel complex in the Stubai region (Alpeiner Valley), compared to data from metapelites in the Oetztal basement to the west, as given in Rode et al. (2012). Sections of the P–T paths are labelled by age data. P–T data from Stubai metapelites and metabasites are interpreted to combine to a prograde-retrograde P–T path. Segments of the P–T path are marked: 1—Age data and minimum P estimate (~ 15 kbar, ellipsoid) from eclogites in Miller and Thöni (1995); they give maximal P at ~ 27 kbar. 2, 3, 4—Positions of EMP monazite age data reported here from Stubai. It is questionable if the metapelites have experienced the high pressures reported from eclogites (1). Stability fields for kyanite, andalusite, sillimanite after Spear (1993). Stability fields of monazite (Mnz) and allanite (Aln) at different bulk rock contents as a function of Ca wt%, and with the xenotime (Xtm) stability field (Janots et al. 2007; Spear 2010). **b** Frequency distribution (recalculated to percent) of the EMP-Th–U–Pb monazite ages in the Oetztal regions to the W, as reported in Rode et al. (2012). **c** Frequency distribution (recalculated to percent) of the EMP-Th–U–Pb monazite ages from the Stubai region (Alpeiner Valley), compared to Oetztal

from garnet metapelites in the Sellrain and Umhausen areas to the NW outside of the Cretaceous chloritoid isograde, and from Sölden and Stubai within this isograde are quite similar (Rode et al. 2012). Also, the monazite ages in all these regions are predominantly Carboniferous. There is yet no indication of a distinct Cretaceous monazite population in the overprinted Oetztal-Stubai basement to the NW of the Schneeberg Complex. Thöny et al. (2008), and Rode et al. (2012) reported no significant quantity of Cretaceous monazite populations from the Winnebach migmatites and from the metapelites to the E of Sölden. In contrast, distinct Permian and Cretaceous monazite populations were described from the overprinted Austroalpine basement to the S of the Tauern Window (Krenn et al. 2012) and from the Saualpe (Schulz 2017). Thus it appears

as reasonable that the amphibolite-facies P–T paths in the OSC are related to the Carboniferous monazite ages.

However, despite the predominant Carboniferous age populations, there are significant differences in monazite microstructures in the Oetztal and Stubai metapelites. Monazites with apatite and allanite coronas are lacking in the Umhausen and Sellrain samples (Rode et al. 2012), and the monazite clusters are only observed in sample RZ31 from Stubai. The monazite phase stability limits may provide some aspects and a clue in this discussion. Studies in amphibolite-facies metapelites have identified a major pulse of monazite growth, which could be linked to the breakdown of garnet at decreasing pressure (Pyle and Spear 1999; Pyle et al. 2001; Spear 2010). In fact, the P–T record in the metapelite garnet ceased during decompression. This could explain the strong variation of Y in monazite which crystallized subsequent to the garnet and which could have incorporated the Y from decomposing garnet. According to Janots et al. (2007), Spear (2010), Spear and Pyle (2010) and Goswami-Banerjee and Robyr (2015), monazite is stable under amphibolite-facies conditions. The temperature-dependent univariant allanite-monazite equilibrium with the monazite stability limit is qualitatively shifted toward lower temperature with decreasing Ca and increasing Al in the bulk rock (Fig. 9a). Within this frame, monazite should have crystallized when the actual P–T path passed the allanite-monazite stability limit at decreasing pressure (Fig. 9a). This implicates that the Schrankogel complex monazite started to crystallise, when the decompression P–T path passed from the kyanite to the sillimanite stability field (Fig. 9a). If this is accepted, the P–T evolution within the kyanite and sillimanite stability fields should be also Carboniferous in the Schrankogel complex, as was similarily reported from the adjacent Sellrain, Umhausen and Sölden micaschists (Rode et al. 2012).

When compared to the monazite age data from the Sellrain, Umhausen and Sölden regions (Rode et al. 2012), with their unimodal age distributions around 317 ± 5 Ma and almost lacking Permian ages, the histograms and isochrones in the Schrankogel complex apparently may indicate a distinct Permian thermal event (Figs. 5b-d, 6b, c). However, this differs considerably from the situation in the Austroalpine basement to the south of the Tauern Window, where the Permian monazite population is more abundant, especially in areas with Permian pegmatites (Krenn et al. 2012). In the Schrankogel complex, the minor population of Permian monazites rather crystallised when the P–T path entered the andalusite stability field at low pressures (Fig. 9a), and apparently does not indicate a separate Permian thermal event.

Double corona structures with apatite and allanite around relic Paleozoic monazites were reported as a characteristic feature of retrogressed basement areas which were overprinted by Alpine (Cretaceous) metamorphism (Finger et al. 1998; 2016; Schulz 2017). Apatite-allanite corona structures around Carboniferous monazite (Fig. 3d–f, i, k) are interpreted as an indicator for monazite decomposition. The corona formation can be explained by pseudomorphic partial replacement of the original monazite by apatite and allanite via a fluid-mediated coupled dissolution–precipitation process (Harlov et al. 2011; Budzyń et al. 2011). At the present stage of knowledge, such monazite corona structures are generated during decreasing pressure and temperature (Broska and Siman 1998; Finger et al. 1998; Krenn and Finger 2007; Budzyń et al. 2011; 2017), and retrogression (Upadhyay and Pruseth 2012). However, an alternative explanation is possible: The micaschists appear as m-scale layers and lenses in a matrix of metabasites which are comparably Ca-rich and may serve as a source for Ca-metasomatism. An increase of bulk rock Ca in the metapelites by metasomatism would shift the monazite stability field toward higher temperatures and would cause monazite dissolution without a significant decrease of temperatures.

The arrangement of cluster monazite (Fig. 5g, h) is distinct from the satellite monazite structure as it was described by Finger et al. (2016). The satellite monazite microstructures are small grains arranged around a larger central grain. It is considered as the new crystallization of small monazite at the rim and in the core of apatite in a former apatite-allanite double corona structure, when monazite stability conditions are attained by re-increasing temperature after a retrogression. At the present limited stage of knowledge about this structure, the cluster monazite at Stubai represents at least a period of new Carboniferous monazite crystallization. In an opposite way as has been outlined above, in this case a decrease of bulk rock Ca, or an increase of bulk rock Al could shift the monazite stability field toward lower temperatures which would result in new monazite crystallisation.

The Schrankogel area is situated within the Alpine chloritoid zone and next to the boundary of Alpine (Cretaceous) biotite cooling ages (Fig. 1b). One can expect temperatures of 350 - 400 °C in this situation. This would be outside the typical temperatures where metamorphic monazite in a Ca-poor and Al-rich bulk rock composition crystallises (Fig. 9a). The Cretaceous temperatures at given pressures may have been simply too low for the given bulk rock Ca contents to allow significant monazite crystallization in this part of the OSC. This could explain the retrogressive corona structures in combination with the completely lacking Cretaceous monazite ages.

8 Conclusions

The nature and geodynamic significance of a Permian event in the Austroalpine and also Southalpine basement units has been increasingly discussed with the emerging new age data and the re-interpretation of existing data (Schuster et al. 2001; Kunz et al. 2018). According to Schuster and Stüwe (2008), the Permian event can be related to (1) intrusion of Permian gabbros into the middle and lower crust, (2) granite and pegmatite intrusions at mid-crustal levels, (3) quartz-andalusite veins and (4) Permian volcanics. Permian metamorphic and magmatic ages, and also monazite ages have yet been mainly reported from Austroalpine basement domains where numerous intrusions of Permian pegmatites occur (Schuster et al. 2001; Schuster and Stüwe 2008, and references therein; Krenn et al. 2012; Schulz 2017). Evidently, the fluid activity associated to these intrusions enhanced the monazite crystallization in metapelites, when low pressure and low bulk Ca compositions are given. In such regions, a Permian monazite population supports the presence of a distinct Permian event. There are yet no own observations or reports of pegmatites and Permian pegmatites respectively from the Alpeiner Valley and the OSC nearby (Klötzli-Chowanetz 2016; Palzer 2016). An important geological marker of a Permian event is therefore lacking in this part of the Austroalpine basement.

In the Schrankogel complex of the Stubai region one observes a clockwise P–T evolution with maximum pressures and temperatures ranging in the high pressure amphibolite facies. This P–T path matches P–T data from metapelites in other parts of the OSC (Rode et al. 2012). Also the predominant Carboniferous monazite populations in 4 metapelite samples are comparable to observations in other parts of the OSC. By comparison of the P–T path to the monazite stability fields at various bulk rock Ca and Al contents it can be concluded that the Carboniferous monazites started to crystallise during decompression after the pressure maximum. A continuing crystallisation of successively younger monazites, often in cluster microstructures, occurred during further decompression within the sillimanite stability field. When the P–T path passed into the andalusite stability field, the conditions for monazite crystallisation even for elevated bulk rock Ca compositions maintained and may have led to a minor population of Permian monazites. These few monazite ages provide no substantial argument for a distinct Permian thermal event in this part of the Austroalpine basement. Also other geological features of such an event are lacking. The Cretaceous metamorphic overprint in this part of the OSC appears as a retrogressive event, which is documented by double corona allanite-apatite structures around relic Carboniferous monazite. No monazite grains with Cretaceous ages are observed in this part of the OSC, as the monazite stability field has not been approached during the Cretaceous overprint. In consequence, the EMP monazite ages from the Oetztal-Stubai area allow to exclude a distinct Permian event in this part of the Austroalpine basement. As exemplified in other parts of this basement with Carboniferous-to-Cretaceous mica mixing ages (Krenn et al. 2012) a Permian event can be discriminated by a corresponding monazite population.

Acknowledgements The electron-microprobe silicate analyses were performed during sessions with technical assistance through D. Heger, Institut für Werkstoffwissenschaft der TU Bergakademie Freiberg. Support at the SEM studies in the Laboratory of Geometallurgy at Freiberg was provided by K. Bachmann and S. Gilbricht. R. Zimmermann thanks the team of Franz-Senn Hütte for hospitality during field work in 2013. The detailed and useful comments provided by B. Budzyń, I. Broska, J. M. Allaz and anonymous reviewers to various versions of the manuscript, and the editorial efforts are gratefully acknowledged.

References

Allaz, J. M. (2017). Testing a new electron microprobe and developing new analytical protocols. *Microscopy Microanalysis, 23*(Suppl. 1), 1052–1053. https://doi.org/10.1017/S143192761700592X.

Bhattacharya, A., Mohanty, L., Maji, A., Sen, S. K., & Raith, M. (1992). Non-ideal mixing in the phlogopite-annite binary: constraints from experimental data on Fe-Mg partitioning and a reformulation of the garnet-biotite geothermometer. *Contributions to Mineralogy and Petrology, 111,* 87–93.

Broska, I., & Siman, P. (1998). The breakdown of monazite in the West-Capathian Veporic orthogneisses and Tatric granites. *Geologica Carpathica, 49,* 161–167.

Budzyń, B., Harlov, D. E., Kozub-Budzyń, G. A., & Majka, J. (2017). Experimental constraints on the relative stabilities of the two systems monazite-(Ce)–allanite-(Ce)–fluorapatite and xenotime-(Y)–(Y, HREE)-rich epidote–(Y, HREE)-rich fluorapatite, in high Ca and Na-Ca environments under P-T conditions of 200–1000 MPa and 450–750 °C. *Mineralogy and Petrology, 111,* 183–217. https://doi.org/10.1007/s00710-016-0464-0.

Budzyń, B., Harlov, D. E., Williams, M. L., & Jercinovic, M. J. (2011). Experimental determination of stability relations between monazite, fluorapatite, allanite, and REE-epidote as a function of pressure, temperature, and fluid composition. *American Mineralogist, 96,* 1547–1567. https://doi.org/10.2138/am.2011.3741.

Cardozo, N., & Allmendinger, R. W. (2013). Spherical projections with OSXStereonet. *Computers & Geosciences, 51,* 193–205. https://doi.org/10.1016/j.cageo.2012.07.021.

Egger, H. (1997). Das sinistrale Innsbruck-Salzburg-Amstetten-Blattverschiebungssystem: Ein weiterer Beleg für die miozäne laterale Extrusion der Ostalpen. *Jahrbuch der Geologischen Bundesanstalt, 140*(1), 47–50.

Egglseder, M., & Fügenschuh, B. (2013). Pre-Alpine fold interference pattern in the northeastern Oetztal-Stubai Complex (Tyrol, Austria). *Austrian Journal of Earth Sciences, 106*(2), 63–74.

Fandrich, R., Gu, Y., Burrows, D., & Moeller, K. (2007). Modern SEM-based mineral liberation analysis. *International Journal of*

Mineral Processing, 84, 310–320. https://doi.org/10.1016/j.minpro.2006.07.018.

Finger, F., Broska, I., Roberts, M., & Schermaier, A. (1998). Replacement of primary monazite by allanite-epidote coronas in an amphibolite-facies granite gneiss from the eastern Alps. *American Mineralogist, 83,* 248–258. https://doi.org/10.2138/am-1998-3-408.

Finger, F., Krenn, E., Schulz, B., Harlov, D. E., & Schiller, D. (2016). Satellite monazites in polymetamorphic basement rocks of the Alps: Their origin and petrological significance. *American Mineralogist, 101,* 1094–1103. https://doi.org/10.2138/am-2016-5477.

Frank, W., Kralik, M., Scharbert, S., & Thöni, M. (1987). Geochronological data from the Eastern Alps. In H. W. Flügel & P. Faupl (Eds.), *Geodynamics of the Eastern Alps* (pp. 272–281). Wien: Deuticke Verlag.

Frey, M., Desmons, J., & Neubauer, F. (1999). The new metamorphic map of the Alps. *Swiss Bulletin of Mineralogy and Petrology, 79,* 1–4.

Frisch, W., Dunkl, I., & Kuhlemann, J. (2000). Post-collisional orogen-parallel large-scale extension in the Eastern Alps. *Tectonophysics, 327,* 239–265. https://doi.org/10.1016/S0040-1951(00)00204-3.

Ganguly, J., Cheng, W., & Tirone, M. (1996). Thermodynamics of aluminosilicate garnet solid solution: new experimental data, an optimized model, and thermometric applications. *Contributions to Mineralogy and Petrology, 126,* 137–151. https://doi.org/10.1007/s004100050240.

Gerya, T., Perchuk, L., Triboulet, C., Audren, C., & Sezko, A. (1997). Petrology of the Tumanshet zonal metamorphic complex, eastern Sayan. *Petrology, 5*(6), 503–533.

Goswami-Banerjee, G., & Robyr, M. (2015). Pressure and temperature conditions for crystallization of metamorphic allanite and monazite in metapelites: A case study from Miyar Valley (high Himalayan Crystalline of Zanskar, NW India). *Journal of Metamorphic Geology, 33,* 535–556. https://doi.org/10.1111/jmg.12133.

Hammer, W. (1929). *Erläuterungen zur Geologischen Spezialkarte der Republik Österreich Blatt Ötztal (5146)*. Wien: Geologische Bundesanstalt.

Harlov, D. E., Wirth, R., & Hetherington, C. J. (2011). Fluid-mediated partial alteration in monazite: the role of coupled dissolution–reprecipitation in element redistribution and mass transfer. *Contributions to Mineralogy and Petrology, 162,* 329–348. https://doi.org/10.1007/s00410-010-0599-7.

Hauke, M., Froitzheim, N., Nagel, T. J., Miladinova, I., Fassmer, K., Fonseca, R. O. C., et al. (2019). Two high-pressure metamorphic events, Variscan and Alpine, dated by Lu–Hf in an eclogite complex of the Austroalpine nappes (Schobergruppe, Austria). *International Journal of Earth Sciences, 108,* 1317–1331. https://doi.org/10.1007/s00531-019-01708-8.

Hoernes, S., & Hoffer, E. (1973). Der Amphibolitzug des mittleren Ötztales (Tirol). *Veröffentlichungen des Tiroler Landesmuseum Ferdinandeum (Innsbruck), 53,* 159–180.

Hoinkes, G., Koller, F., & Rantitsch, G. (1999). Alpine metamorphism of the Eastern Alps. *Schweizerische Mineralogische und Petrographische Mitteilungen, 79*(1), 155–181.

Hoinkes, G., Kostner, A., & Thöni, M. (1991). Petrologic constraints for Eoalpine eclogite facies metamorphism in the Austroalpine Ötztal basement. *Mineralogy and Petrology, 43,* 237–254.

Hoinkes, G., & Thöni, M. (1993). Evolution of the Ötztal-Stubai, Scarl-Campo and Ulten Basement Units. In J. F. von Raumer & F. Neubauer (Eds.), *The pre-Mesozoic Geology of the Alps* (pp. 485–494). Heidelberg: Springer Verlag.

Holdaway, M. J. (2001). Recalibration of the GASP geobarometer in light of recent garnet and plagioclase activity models and versions of the garnet-biotite geothermometer. *American Mineralogist, 86,* 1117–1129. https://doi.org/10.2138/am-2001-1001.

Holland, T. J. B. (1980). The reaction albite = jadeite + quartz determined experimentally in the range 600–1200°C. *American Mineralogist, 65,* 129–134.

Holland, T. J. B. (1983). The experimental determination of activities in disordered and short-range ordered jadeitic pyroxene. *Contributions to Mineralogy and Petrology, 82,* 214–220.

Holland, T. J. B., & Powell, R. (1998). An internally-consistent thermodynamic dataset for phases of petrological interest. *Journal of Metamorphic Geology, 16,* 309–344.

Janots, E., Brunet, F., Goffé, B., Poinssot, C., Burchard, M., & Cemic, L. (2007). Thermochemistry of monazite-(La) and dis-sakisite-(La): implications for monazite and allanite stability in metapelites. *Contributions to Mineralogy and Petrology, 154,* 1–14. https://doi.org/10.1007/s00410-006-0176-2.

Jarosewich, E., & Boatner, L. A. (1991). Rare-earth element reference samples for electron microprobe analysis. *Geostandards Newsletter, 15,* 397–399.

Jercinovic, M. J., Williams, M. L., & Lane, E. D. (2008). In-situ trace element analysis of monazite and other fine-grained accessory minerals by EMPA. *Chemical Geology, 254,* 197–215. https://doi.org/10.1016/j.chemgeo.2008.05.016.

Klötzli-Chowanetz, E. (2016). Bericht 2014 über geologische Aufnahmen im östlichen Ötztalkristallin auf Blatt 147 Axams. *Jahrbuch der Geologischen Bundesanstalt, 156*(1–4), 270–273.

Klötzli-Chowanetz, E., Klötzli, U., & Koller, F. (1997). Lower Ordovician migmatisation in the Ötztal crystalline basement (Eastern Alps, Austria): Linking U-Pb and Pb-Pb dating with zircon morphology. *Swiss Bulletin of Mineralogy and Petrology, 77,* 315–324.

Klötzli-Chowanetz, E., Klötzli, U., & Skiöld, T. (2001). Cambrian migmatisation and Ordovician tonalitic intrusion—Klopaier area, Ötztal crystalline complex, Eastern Alps. *Mitteilungen der Österreichischen Mineralogischen Gesellschaft, 146,* 133–134.

Krenn, E., & Finger, F. (2007). Formation of monazite and rhabdophane at the expense of allanite during Alpine low temperature retrogression of metapelitic basement rocks from Crete, Greece: Microprobe data and geochronological implications. *Lithos, 95,* 130–147. https://doi.org/10.1016/j.lithos.2006.07.007.

Krenn, E., Schulz, B., & Finger, F. (2012). Three generations of monazite in Austroalpine basement rocks to the south of the Tauern Window—Evidences for Variscan, Permian and Alpine metamorphism. *Swiss Journal of Geosciences, 105,* 343–360. https://doi.org/10.1007/s00015-012-0104-6.

Kunz, B. E., Manzotti, P., von Niederhäusern, B., Engi, M., Darling, J. R., Giuntoli, F., et al. (2018). Permian high-temperature metamorphism in the Western Alps (NW Italy). *International Journal of Earth Sciences (Geologische Rundschau), 107,* 203–218. https://doi.org/10.1007/s00531-017-1485-6.

Leake, B. E., Woolley, A. R., Arps, C. E., Birch, W. D., Gilbert, M. C., Grice, J. D., et al. (1997). Nomenclature of Amphiboles: Report of the subcommittee in amphiboles of the International Mineralogical Association, commission on new minerals and mineral names. *The Canadian Mineralogist, 35,* 219–246.

Ludwig, K. (2001). *Users manual for Isoplot/Ex (rev. 2.49): A geochronological toolkit for Microsoft Excel*. Berkeley: Berkeley Geochronological Center.

Marotta, A. M., & Spalla, M. I. (2007). Permian-Triassic high thermal regime in the Alps: Result of late Variscan collapse or continental rifting? Validation by numerical modeling. *Tectonics, 26,* TC4016. https://doi.org/10.1029/2006TC002047.

Miller, D. S., Jäger, E., & Schmidt, K. (1967). Rb-Sr-Altersbestimmungen an Biotiten der Raibler Schichten des Brennermesozoikums und am Muscovitgneis von Vent (Ötztaler Alpen). *Eclogae Geologicae Helveticae, 60,* 537–541. https://doi.org/10.5169/seals-163498.

Miller, C., & Thöni, M. (1995). Origin of eclogites from the Austroalpine Ötztal basement (Tirol, Austria): Geochemistry and Sm-Nd vs. Rb-Sr isotope systematics. *Chemical Geology, 122,* 199–225.

Mogessie, A., & Purtscheller, F. (1986). Polymetamorphism of the Oetztal-Stubai basement complex based on amphibolite petrology. *Jahrbuch der Geologischen Bundesanstalt Wien, 129,* 69–91.

Mogessie, A., Purtscheller, F., & Tessadri, R. (1985). Geochemistry of amphibolites from the Ötztal-Stubai Complex (Northern Tyrol, Austria). *Chemical Geology, 51,* 103–113.

Montel, J., Foret, S., Veschambre, M., Nicollet, C., & Provost, A. (1996). A fast, reliable, inexpensive in situ dating technique: Electron microprobe ages on monazite. *Chemical Geology, 131,* 37–53.

Neubauer, F., Hoinkes, G., & Sassi, F. P. (1999). Pre-Alpine metamorphism of the Eastern Alps. *Swiss Bulletin of Mineralogy and Petrology, 79*(1), 41–62.

Osbahr, I., Krause, J., Bachmann, K., & Gutzmer, J. (2015). Efficient and accurate identification of Platinum-Group Minerals by a combination of mineral liberation and electron probe microanalysis with a new approach to the offline overlap correction of Platinum-Group Element concentrations. *Microscopy and Microanalysis, 21,* 1–16. https://doi.org/10.1017/S1431927615000719.

Palzer, M. (2016). Bericht 2014 über kristallingeologische Aufnahmen im Bereich Franz-Senn-Hütte und Bassler Joch auf Blatt 147 Axams. *Jahrbuch der Geologischen Bundesanstalt, 156*(1–4), 273–278.

Parrish, R. R. (1990). U-Pb dating of monazite and its application to geological problems. *Canadian Journal Earth Sciences, 27,* 1431–1450. https://doi.org/10.1139/e90-152.

Powell, R., & Holland, T. J. B. (1993). On the formulation of simple mixing models for complex phases. *American Mineralogist, 78,* 1174–1180.

Purtscheller, F. (1978). *Ötztaler und Stubaier Alpen Sammlung Geologischer Führer* (vol. 53, 2nd edn., pp. 128). Gebrüder Bornträger, Stuttgart.

Pyle, J. M., & Spear, F. S. (1999). Yttrium zoning in garnet: Coupling of major and accessory phases during metamorphic reactions. *Geological Materials Research, 1*(6), 1–49.

Pyle, J. M., Spear, F. S., Rudnick, R., & McDonough, W. (2001). Monazite-xenotime-garnet equilibrium in metapelites and a new monazite-garnet thermometer. *Journal of Petrology, 42,* 2083–2107.

Pyle, J. M., Spear, F. S., Wark, D. A., Daniel, C. G., & Storm, L. C. (2005). Contributions to precision and accuracy of chemical ages of monazite. *American Mineralogist, 90,* 547–577. https://doi.org/10.2138/am.2005.1340.

Ramsay, J. G., & Huber, M. (1987). *Techniques of Modern Structural Geology, Vol. 2: Folds and Fractures* (pp. 392). London: Academic Press.

Ratschbacher, L., Frisch, W., Linzer, H. G., & Merle, O. (1991). Lateral extrusion in the Eastern Alps, Part 2: Structural analysis. *Tectonics, 10*(2), 257–271.

Rode, S., Rösel, D., & Schulz, B. (2012). Constraints on the Variscan P-T evolution by EMP Th-U-Pb monazite dating in the polymetamorphic Austroalpine Oetztal-Stubai basement (Eastern Alps). *German Journal of Geology (Zeitschrift der deutschen Gesellschaft für Geowissenschaften), 163*(1), 43–68. https://doi.org/10.1127/1860-1804/2012/0163-0043.

Schindlmayr, A. (1999). Granitoids and plutonic evolution of the Ötztal-Stubai Massif. Ph.D. Dissertation, Universität Salzburg at Salzburg, Austria.

Schmid, S., Fügenschuh, B., Kissling, E., & Schuster, R. (2004). Tectonic map and overall architecture of the Alpine orogen. *Eclogae Geologicae Helvetiae, 97,* 93–117. https://doi.org/10.1007/s00015-004-1113-x.

Schmidegg, O. (1964). Die Ötztaler Schubmasse und ihre Umgebung. *Verhandlungen der Geologischen Bundesanstalt Wien, 1964*(1), 27–47.

Schulz, B. (1994). Polyphase Variscan P-T-deformation path from mica schists of the sillimanite zone in the Austroalpine Ötztal-Stubai basement (Eastern Alps). *Neues Jahrbuch für Mineralogie Abhandlungen, 168,* 47–65.

Schulz, B. (2014). Early Carboniferous P-T path from the Upper Gneiss Unit of Haut-Allier (French Massif Central)—reconstructed by geothermobarometry and EMP-Th-U-Pb monazite dating. *Journal of Geosciences, 59,* 327–349. https://doi.org/10.3190/Jgeosci.178.

Schulz, B. (2017). Polymetamorphism in garnet micaschists of the Saualpe Eclogite Unit (Eastern Alps, Austria), resolved by automated SEM methods and EMP-Th-U-Pb monazite dating. *Journal of Metamorphic Geology, 35*(2), 141–163. https://doi.org/10.1111/jmg.12224.

Schulz, B., & Schüssler, U. (2013). Electron-microprobe Th-U-Pb monazite dating in Early-Palaeozoic high-grade gneisses as a completion of U-Pb isotopic ages (Wilson Terrane, Antarctica). *Lithos, 175–176,* 178–192. https://doi.org/10.1016/j.lithos.2013.05.008.

Schulz, B., Steenken, A., & Siegesmund, S. (2008). Geodynamics of an Alpine terrane— the Austroalpine basement to the south of the Tauern Window as a part of the Adriatic Plate. In S. Siegesmund, B. Fügenschuh & N. Froitzheim (Eds.) *Tectonic Aspects of the Alpine-Dinaride-Carpathian System* (vol. 298, pp. 5–43). London: Geological Society of London Special Publications.

Schuster, R., Scharbert, S., Abart, R., & Frank, W. (2001). Permo-Triassic extension and related HT/LP metamorphism in the Austroalpine—South Alpine realm. *Mitteilungen Geologie und Bergbaustudenten Österreich, 44,* 111–141.

Schuster, R., & Stüwe, K. (2008). Permian metamorphic event in the Alps. *Geology, 36/8,* 603–606. https://doi.org/10.1130/G24703A.1.

Söllner, F. (2001). The Winnebach migmatite (Ötz-Stubai crystalline unit)—Evidence for a Pan-African metamorphism in an overthrust nappe sequence in the Eastern Alps. *Geologische und Paläontologische Mitteilungen der Universität Innsbruck, 25,* 199–200.

Spear, F. S. (1993). *Metamorphic phase equilibria and pressure-temperature-time paths. Mineralogical Society of America Monography Series No. 1* (pp. 799). Washington D. C.: Mineralogical Society of America.

Spear, F. S. (2010). Monazite-allanite phase relations in metapelites. *Chemical Geology, 279*(1-2), 55–62. https://doi.org/10.1016/j.chemgeo.2010.10.004.

Spear, F. S., & Pyle, J. (2002). Apatite, monazite and xenotime in metamorphic rocks. *Reviews in Mineralogy and Geochemistry, 48/1,* 293–335. https://doi.org/10.2138/rmg.2002.48.7.

Spear, F. S., & Pyle, J. M. (2010). Theoretical modeling of monazite growth in a low-Ca metapelite. *Chemical Geology, 273,* 111–119. https://doi.org/10.1016/j.chemgeo.2010.02.016.

Spear, F. S., Pyle, J. M., & Cherniak, D. (2009). Limitations of chemical dating of monazite. *Chemical Geology, 266,* 218–230. https://doi.org/10.1016/j.chemgeo.2009.06.007.

Suzuki, K., & Adachi, M. (1991). Precambrian provenance and Silurian metamorphism of the Tsunosawa paragneiss in the

South Kitakami terrane, Northeast Japan, revealed by the chemical Th-U-total Pb isochron ages of monazite, zircon and xenotime. *Geochemical Journal, 25,* 357–376.

Suzuki, K., Adachi, M., & Kajizuka, I. (1994). Electron microprobe observations of Pb diffusion in metamorphosed detrital monazites. *Earth and Planetary Science Letters, 128,* 391–405.

Suzuki, K., & Kato, T. (2008). CHIME dating of monazite, xenotime, zircon and polycrase: Protocol, pitfalls and chemical criterion of possible discordant age data. *Gondwana Research, 14,* 569–586. https://doi.org/10.1016/j.gr.2008.01.005.

Thöni, M. (1981). Degree and Evolution of the Alpine Metamorphism in the Austroalpine Unit W of Hohe Tauern in the light of K/Ar and Rb/Sr Age Determinations in Micas. *Jahrbuch der Geologischen Bundesanstalt Wien, 124,* 111–174.

Thöni, M. (1983). The climax of the early Alpine metamorphism in the Austroalpine thrust sheet. *Memorie Science Geologiche Padova, 36,* 211–238.

Thöni, M. (1999). A review of geochronological data from the Eastern Alps. *Swiss Bulletin of Mineralogy and Petrology, 79*(1), 209–230.

Thöny, W. F., Tropper, P., Schennach, F., Krenn, E., Finger, F., Kaindl, R., et al. (2008). The metamorphic evolution of migmatites from the Ötztal Complex (Tyrol, Austria) and constraints on the timing of the pre-Variscan high-T event in the Eastern Alps. *Swiss Journal of Geosciences, 101*(Supplement 1), 111–126. https://doi.org/10.1007/s00015-008-1290-0.

Tropper, P., & Hoinkes, G. (1996). Geothermobarometry of Al_2SiO_5-bearing metapelites in the western Austroalpine Ötztal-basement. *Mineralogy and Petrology, 58,* 145–170.

Tropper, P., & Recheis, A. (2003). Garnet zoning as a window into the metamorphic evolution of a crystalline complex: The northern and central Austroalpine Ötztal-Complex as a polymorphic example. *Mitteilungen der Österreichischen Geologischen Gesellschaft, 94,* 27–53.

Upadhyay, D., & Pruseth, K. L. (2012). Fluid-induced dissolution breakdown of monazite from Tso Morari complex, NW Himalayas: Evidence for immobility of trace elements. *Contributions to Mineralogy and Petrology, 164,* 303–316. https://doi.org/10.1007/s00410-012-0739-3.

Williams, M. L., Jercinovic, M. J., Mahan, K. H., & Dumond, G. (2017). Electron microprobe petrochronology. *Reviews in Mineralogy and Geochemistry, 83,* 153–182. https://doi.org/10.1515/9783110561890-006.

Wu, C. M. (2015). Revised empirical garnet-biotite-muscovite-plagioclase (GBMP) geobarometer in metapelites. *Journal of Metamorphic Geology, 33,* 167–176. https://doi.org/10.1111/jmg.12115.

Wu, C. M., Zhang, J., & Ren, L. D. (2004). Empirical garnet-biotite-plagioclase-quartz (GBPQ) geobarometry in medium- to high-grade metapelites. *Journal of Petrology, 45*(9), 1907–1921.

Zenk, M., & Schulz, B. (2004). Zoned Ca-amphiboles and related P-T evolution in metabasites from the classical Barrovian metamorphic zones in Scotland. *Mineralogical Magazine, 68*(5), 769–786. https://doi.org/10.1180/0026461046850218.